

Fundamentals of the dwarf fundamental plane [★]

Marshall L. McCall¹, O. Vaduvescu^{2,3}, F. Pozo Nunez³, A. Barr Dominguez³, R. Fingerhut¹, E. Unda-Sanzana³, Bintao Li¹, and M. Albrecht^{4,3}

¹ York University, Department of Physics and Astronomy, 4700 Keele Street, Toronto, ON, Canada M3J1P3
e-mail: mccall@yorku.ca

² Isaac Newton Group of Telescopes, Ap. de correos 321, E-38700 Santa Cruz de la Palma, Canary Islands, Spain
e-mail: ovidiuv@ing.iac.es

³ Instituto de Astronomía, Universidad Católica del Norte, Avenida Angamos 0610, Antofagasta, Chile

⁴ Argelander-Institut für Astronomie, Universität Bonn, Auf dem Hügel 71, 53121 Bonn, Germany

Received 08 July 2011; Accepted 27 January 2012

ABSTRACT

Aims. Star-forming dwarfs are studied to elucidate the physical underpinnings of their fundamental plane. Processes controlling dynamics are evaluated, connections between quiescent and bursting dwarfs are examined, and the viability of using structural properties of dwarfs to determine distances is assessed.

Methods. Deep surface photometry in K_s is presented for 19 star-forming dwarfs. The data are amalgamated with previously published observations to create a sample of 66 galaxies suitable for exploring how global properties and kinematics are connected.

Results. It is confirmed that residuals in the Tully-Fisher relation are correlated with surface brightness, but that even after accommodating the surface brightness dependence through the dwarf fundamental plane, residuals in absolute magnitude are far larger than expected from observational errors. Rather, a *more* fundamental plane is identified which connects the potential to HI line width and surface brightness. Residuals correlate with the axis ratio in a way which can be accommodated by recognizing the galaxies to be oblate spheroids viewed at varying angles. Correction of surface brightnesses to face-on leads to a correlation among the potential, line width, and surface brightness for which residuals are entirely attributable to observational uncertainties. The mean mass-to-light ratio of the diffuse component of the galaxies is constrained to be 0.88 ± 0.20 in K_s . Blue compact dwarfs lie in the same plane as dwarf irregulars. The dependence of the potential on line width is less strong than expected for virialized systems, but this may be because surface brightness is acting as a proxy for variations in the mass-to-light ratio from galaxy to galaxy. Altogether, the observations suggest that gas motions are predominantly disordered and isotropic, that they are a consequence of gravity, not turbulence, and that the mass and scale of dark matter haloes scale with the amount and distribution of luminous matter. The tight relationship between the potential and observables offers the promise of determining distances to unresolved star-forming dwarfs to an accuracy comparable to that provided by the Tully-Fisher relation for spirals.

Key words. galaxies – dwarf, fundamental parameters, kinematics and dynamics, structure; infrared – galaxies; cosmology – dark matter

1. Introduction

Λ CDM cosmology leads to dwarf galaxies with dark matter haloes at the centre of which is a cusp in density. However, dwarfs in which a significant portion of their internal energy is ordered show rotation curves which rise less steeply outward from their centres than expected. Thus, their core density profiles must be quite flat (Moore 1994; Flores & Primack 1994; Simon et al. 2005; de Blok et al. 2008; Oh et al. 2011, and references therein). Dwarfs over a wide range of absolute magnitudes display surface brightness profiles which are flat in the cores, also suggestive of a central dark matter framework whose density is slowly varying (Vaduvescu et al. 2005). Hydrodynamic simulations taking into account star formation and its consequences suggest that a flat density profile is a response to the

blowout of baryonic matter with low angular momentum by supernova explosions (Governato et al. 2010). On the contrary, the chemical properties of star-forming dwarfs in low-density environments indicate that gas flows have not played a major role in their evolution (Lee et al. 2003; Vaduvescu et al. 2007).

A clue as to whether or not the current state of dwarfs is a consequence of gas flows may come from velocity dispersions. Galaxies whose evolution has been affected significantly by flows may well display internal motions which are not entirely explainable as a response to gravity. Recently, rotating disk galaxies were discovered at low redshift in which the velocity dispersion is large (Green et al. 2010). Because line widths correlate with star formation rates but not masses or gas fractions, the unusual motions were attributed to turbulence resulting from star formation activity. This may be relevant to understanding the Tully-Fisher relation for star-forming dwarfs, which is highly scattered (Vaduvescu & McCall 2008). Although some of the scatter can be explained through a connection to surface

Send offprint requests to: M. L. McCall

[★] Based on observations acquired from CFHT, CTIO, ESO, OAN-SPM, and SAAO

brightness (the fundamental plane for dwarfs), there remains a significant component which cannot be attributed to observational errors (Vaduvescu & McCall 2008).

Within the context of evaluating the impact of star formation on dynamics, and by implication the evolution of both mass and chemistry, it is important to examine in more detail how closely the mass and distribution of visible matter in dwarfs are linked to kinematics. This motivates, in particular, exploration of the baryonic Tully-Fisher relation (McGaugh et al. 2000), since a significant portion of the mass of star-forming dwarfs is in gaseous form. From the standpoint of turbulence, it is of interest to compare blue compact dwarfs, in which there is evidence for a recent burst of star formation, with the more quiescent dwarf irregular galaxies (e.g., Vaduvescu et al. 2006). A better understanding of the physics of star-forming dwarfs also has the potential to open up new avenues for determining distances. At the moment, distances to unresolved systems are so poorly constrained that it is not possible to map peculiar motions on large scales independently from giants.

In this paper, star-forming dwarfs in the Local Volume whose structural properties are defined by near-infrared surface photometry are employed to study how the luminosity, baryonic mass, and baryonic potential are linked to kinematics. Simultaneously, the mass-to-light ratio is constrained by optimizing linkages. Section 2 introduces new near-infrared observations of star-forming dwarfs, the surface photometry for which is presented in Section 3. An expanded sample of galaxies suitable for study is assembled in Section 4, and then subjected to detailed analysis in Section 5. This leads to the identification of a *more* fundamental plane for dwarfs. Section 6 follows with a discussion of results, especially examining how closely internal motions are tied to gravity. As well, a new method for deriving distances to dwarfs is presented. Finally, conclusions are presented in Section 7.

2. Observations

2.1. Blanco observations 2008

During 2008 Mar 10–13 and Aug 10–12, deep NIR images of 23 galaxies were acquired using the 4.1 m Blanco telescope at Cerro Tololo Inter-American Observatory, Chile (Run IDs: 2008A-0913 and 2008B-0909). All three nights of the first run were photometric, but only the second night of the August run was clear. During both runs, the ISPI camera was used at the $f/8$ Cassegrain focus. The detector was a Hawaii array with 2048×2048 pixels. The scale was $0''.3 \text{ pix}^{-1}$, yielding a field of view $10''.25 \times 10''.25$. Targets were imaged exclusively through the K_s filter. Table 1 summarizes the observations.

To sample the sky, small objects were cycled through four quadrants of the array. For large targets, the telescope was jogged to a sky field after every pair of dithered target images. Data were reduced, calibrated, and analyzed in the manner described by Vaduvescu et al. (2005). Typically, 10 to 15 2MASS stars were employed to calibrate each field. Imaging and surface photometry for the 13 dwarfs clearly detected with the Blanco telescope are presented in Figure 1.

For reference, Figure 2 gives the reduced images of the fields of the 10 unexaminable dwarfs. It is possible that galaxies imaged in August (HIPASS J1337–39, Sag DIG, and DDO 210) were obscured by thin clouds. HIPASS J1351–47 and Sag DIG appear to have been detected, but not well enough to permit surface photometry. The remaining galaxies were just too faint to detect with the chosen exposures.

2.2. NTT observations 2008

During 2008 Aug 13–17, deep NIR imaging of nine galaxies was undertaken with the 3.5 m NTT telescope at ESO La Silla Observatory, Chile (Run ID: 081.B-0386(A)). One night was clear, and the rest were clouded out. The SOFI camera equipped with a Hawaii HgCdTe array was employed at the $f/11$ Nasmyth focus. The array was composed of 1024×1024 pixels. The scale was $0''.288 \text{ pix}^{-1}$, so the field of view was $4''.92 \times 4''.92$. All targets were observed with the K_s filter only. Observations are summarized in Table 1.

Data were reduced, calibrated, and analyzed in the same manner as for the Blanco runs. Around five 2MASS stars were employed to calibrate most of the fields. Imaging and surface photometry for the six dIs solidly detected are included in Figure 1. Figure 2 includes the reduced images of the fields of the two unexaminable dwarfs not observed with the Blanco telescope. In fact, ESO 540-30 appears to have been detected, but not well enough to carry out surface photometry.

2.3. Other observations 2002–2007

As part of separate studies, deep K_s images of 110 different dwarf galaxies were obtained from 2002 to 2007 over observing runs conducted with the 2.1 m telescope of OAN-SPM in Mexico (2002 and 2005), the 1.4 m IRSF telescope of SAAO in South Africa (2005 and 2006), the 3.6 m CFHT in Hawaii (2002, 2004, 2005, and 2006), and the Blanco Telescope at CTIO (2006 and 2007). Images and surface photometry are presented in Vaduvescu et al. (2005) (34 galaxies), Vaduvescu & McCall (2008) (17 galaxies, plus eight from 2MASS), and Fingerhut et al. (2010) (80 galaxies).

3. Surface photometry

Of the newly-observed dwarfs, 15 out of 19 have flat cores and exponential wings. Vaduvescu et al. (2005) showed that a sech function provides a good fit to such profiles. For this function, the apparent surface brightness μ^{app} in mag arcsec $^{-2}$ at radius r along the major axis is given by

$$\mu^{app} = \mu_0^{app} - 2.5 \log \frac{2}{e^{r/r_0} + e^{-r/r_0}} \quad (1)$$

where μ_0^{app} is the apparent surface brightness at the centre and r_0 is the scale length. Solutions for the parameters of the best fitting sech functions are given in Table 2. In the right panels of Figure 1, fits are shown as thick solid lines.

Some dwarfs show an excess of light in their centres. They can be interpreted as being normal dIs hosting a central starburst, i.e., blue compact dwarfs (Vaduvescu et al. 2006). NGC 1311 and ESO 137-18 are two such objects. Their surface brightness profiles were modeled by simultaneously fitting a Gaussian on top of the sech function describing the extended underlying light distribution. In Figure 1, the Gaussian component is displayed as a dashed line, and the sum of the Gaussian and sech functions is marked by a thin solid line.

The brightness of the main body of each dwarf was estimated by integrating the sech function out to infinity. The apparent total magnitude m_{sech}^{app} , referred to here as the *sech magnitude*, was computed from

$$m_{sech}^{app} = -2.5 \log \left[11.51036 r_0^2 q I_0^{app} \right] \quad (2)$$

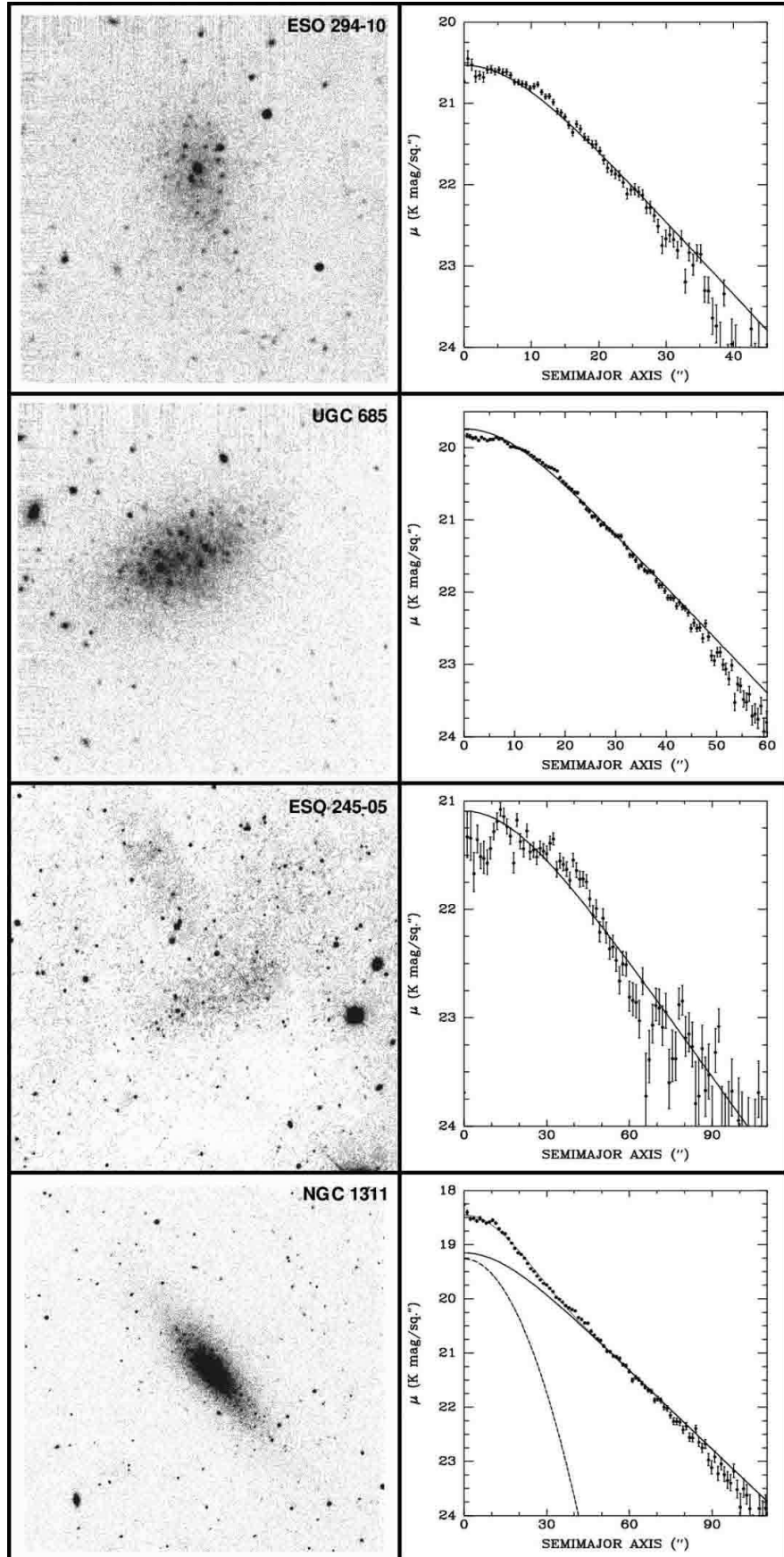


Fig. 1. Images and surface photometry of dIs observed at CTIO (Blanco) and La Silla (NTT). Left panels: K_s images (North is up, East to the left). The field of view is about $5' \times 5'$ (Blanco) or $2.5' \times 2.5'$ (NTT). Right panels: Surface brightness profiles in K_s for the unresolved components. The thick solid curves are fits of a sech function. In a few cases, a Gaussian burst was fitted simultaneously, and is marked by a dashed curve. In these cases, the sum of the sech and Gaussian components is shown as a thin solid line (sometimes hard to see due to overlap with the observations).

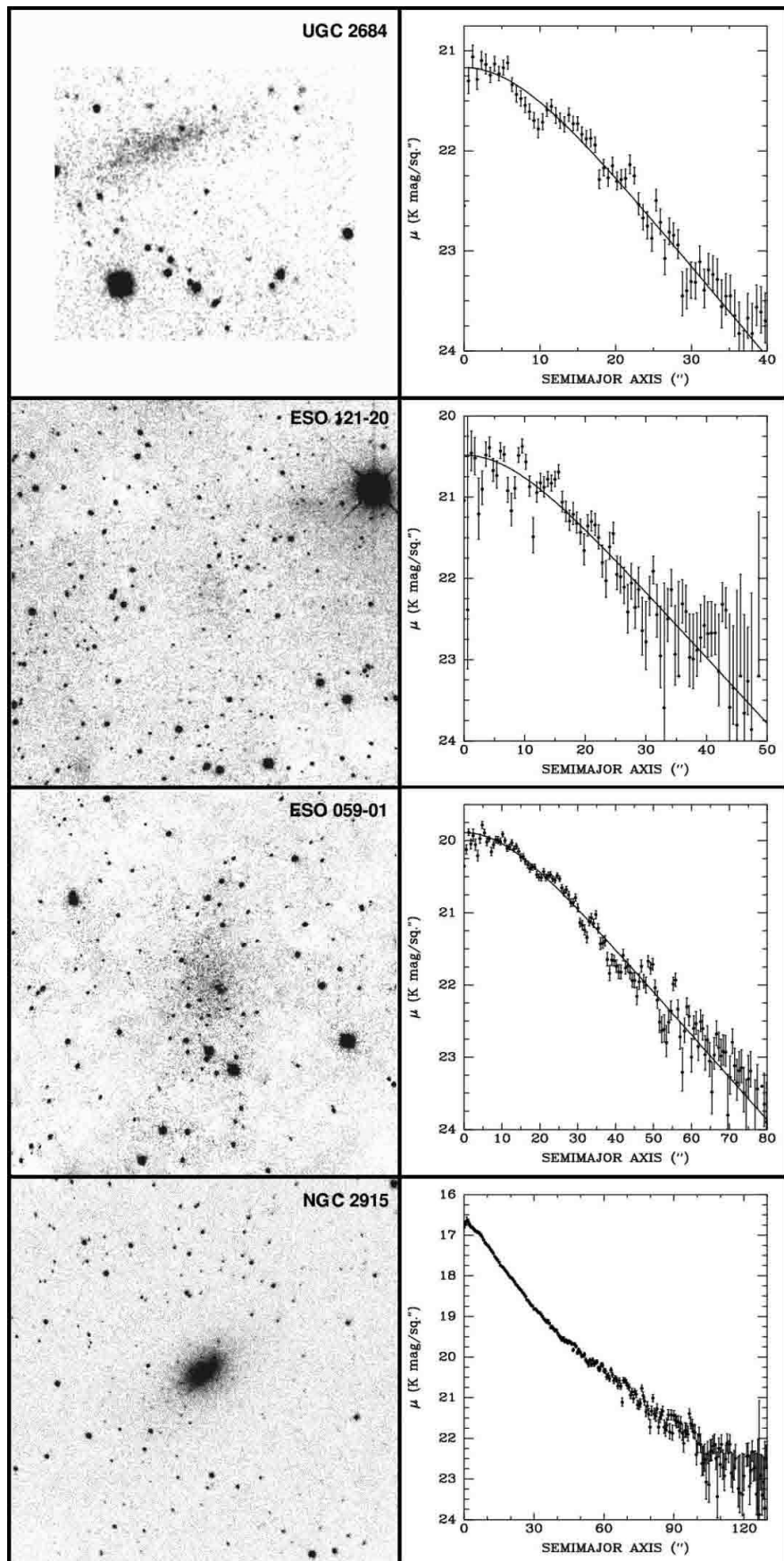


Fig. 1. (cont'd)

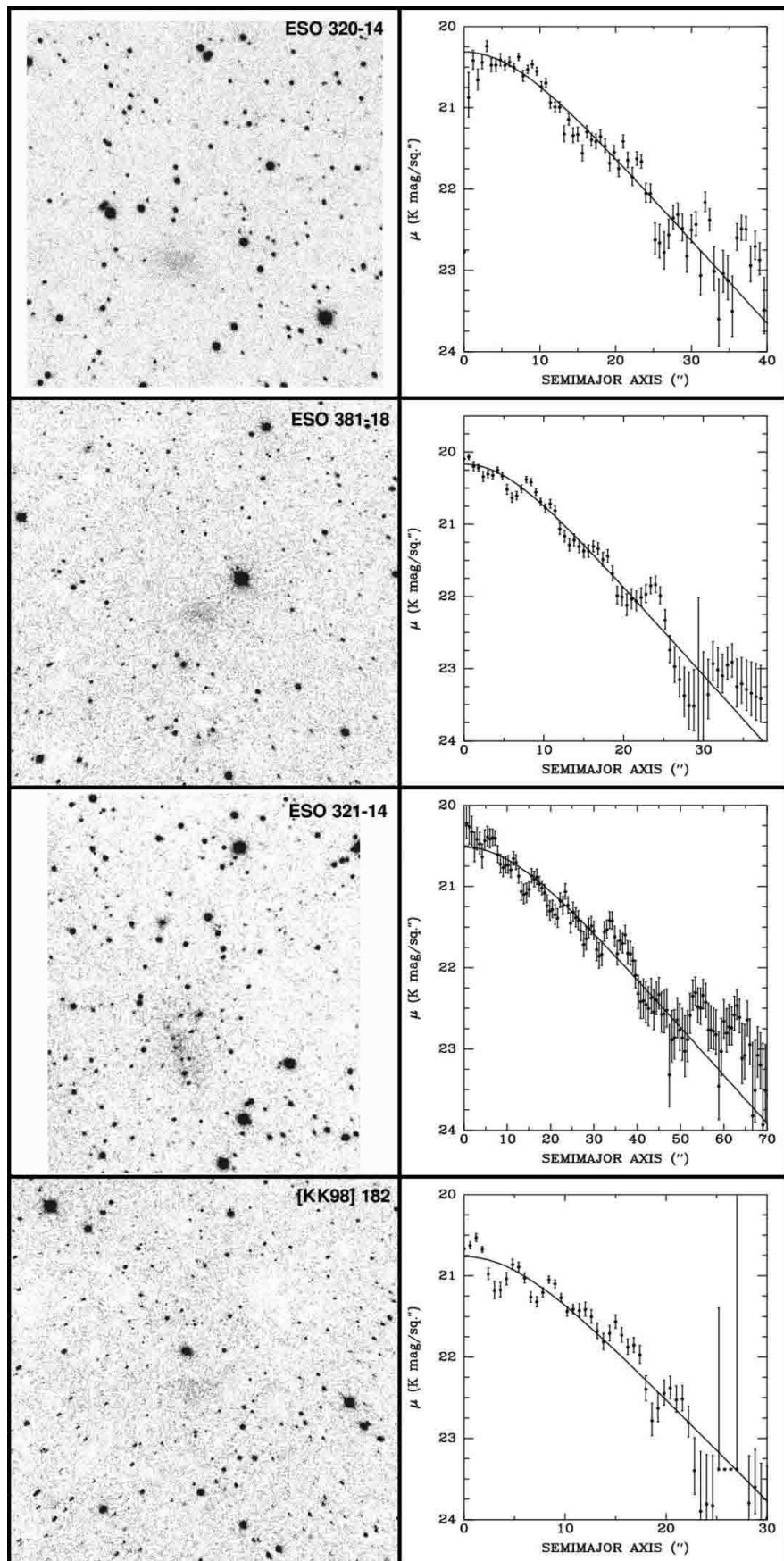


Fig. 1. (cont'd)

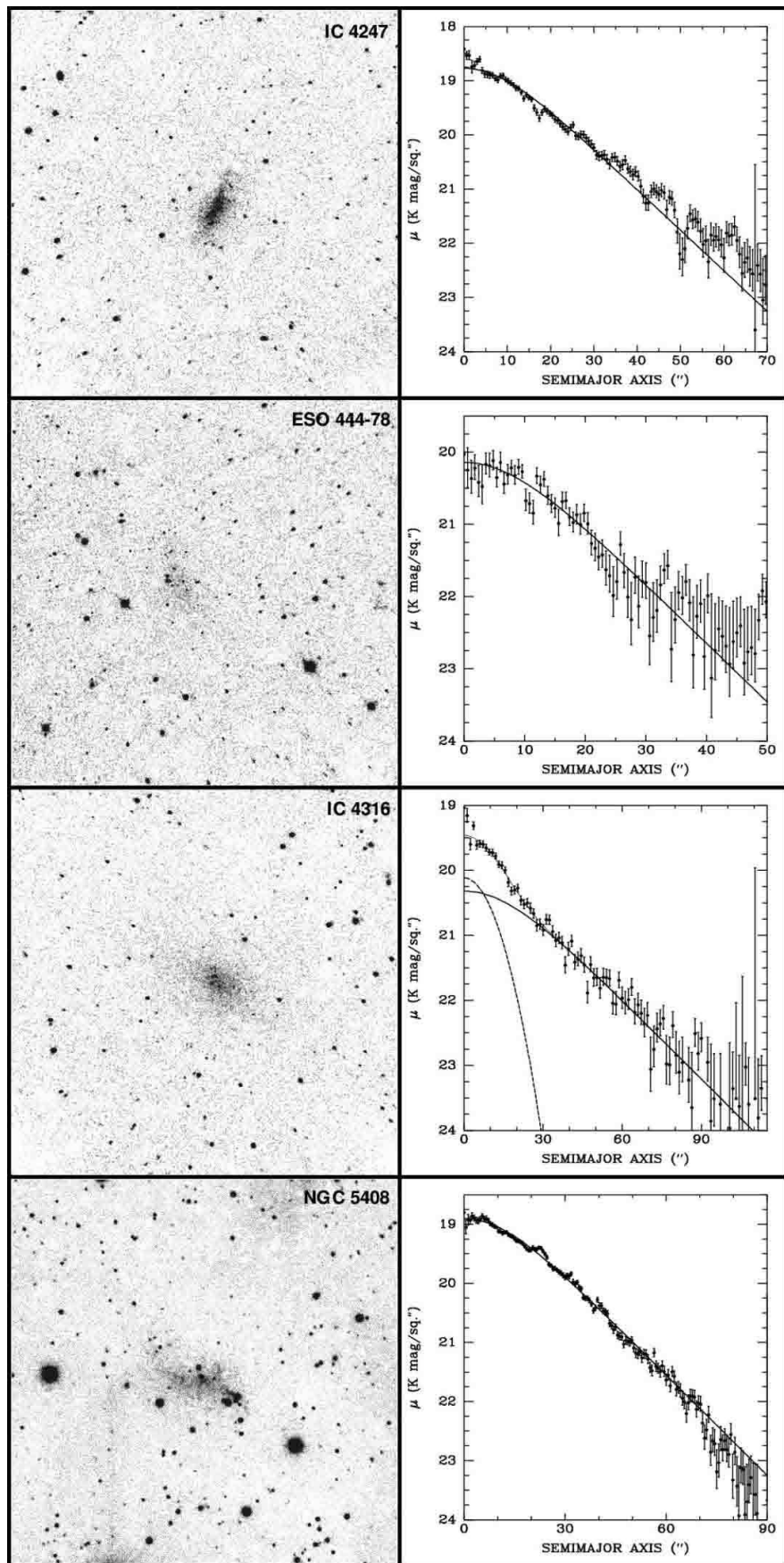
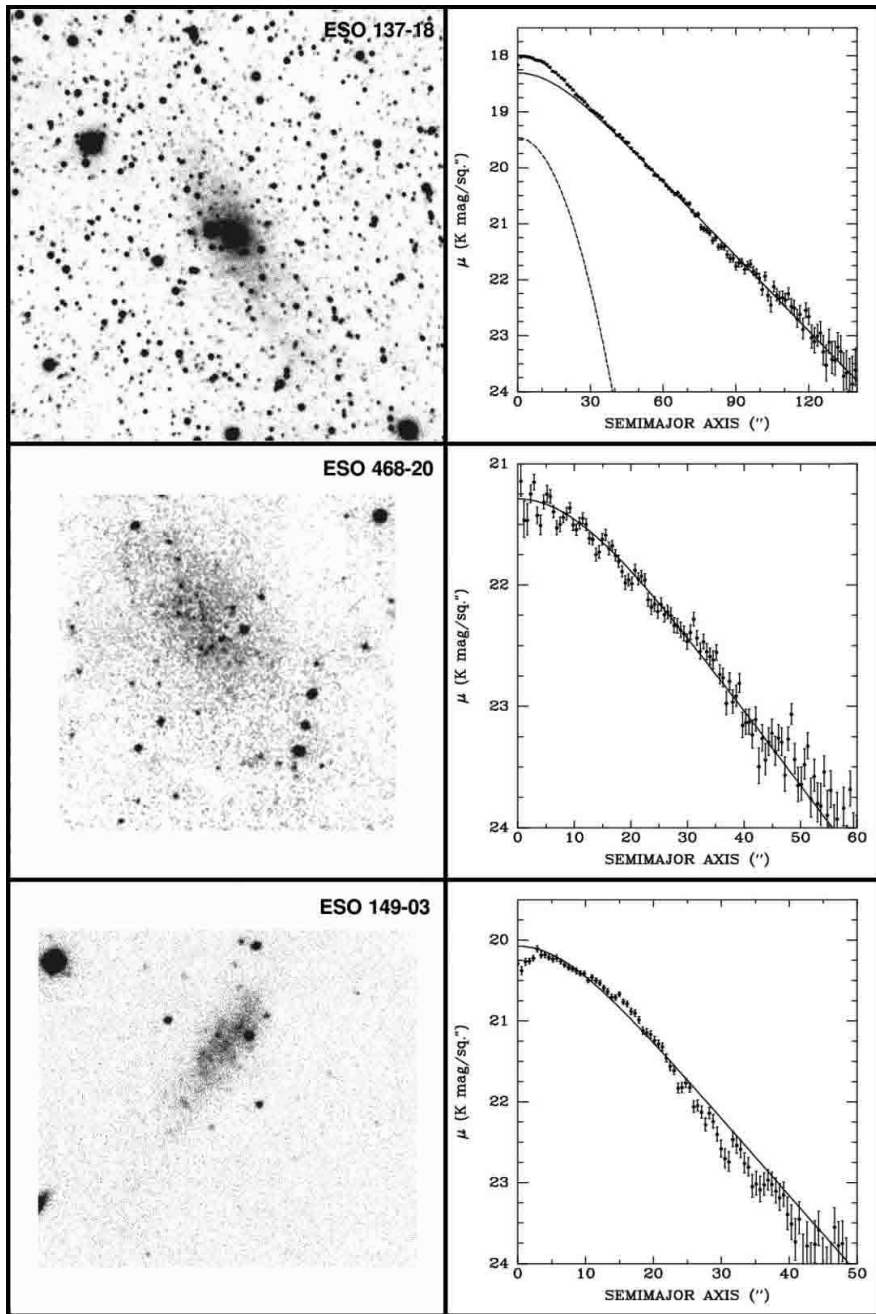


Fig. 1. (cont'd)


Fig. 1. (cont'd)

where I_0^{app} is the apparent central surface brightness in linear units and q is the axis ratio (b/a) of the isophotes. The magnitude within the outermost detected isophote, referred to here as the *isophotal magnitude*, was also estimated. Sech and isophotal magnitudes for all 19 of the dwarfs detected at Blanco and the NTT are given in Table 2.

4. Amalgamated sample and data

The observations presented above and in Fingerhut et al. (2010) significantly expand the sample of dwarfs for which deep K_s -band photometry is available. Thus, it is appropriate to re-examine the scaling relations elucidated earlier, especially to seek deeper insights into the why scatter is so much greater than expected from observational errors.

A sample of star-forming dwarfs was compiled from galaxies with extant K_s -band surface photometry to which a sech profile had been fitted. In order to minimize scatter due to distance errors, the sample was restricted to objects for which the I magnitude and $V - I$ colour of the tip of the red giant branch (TRGB) have been measured reliably. A total of 66 galaxies satisfied the criteria for analysis, and are listed in Table 3. The galaxies IC 10 and ESO 245-05 were not included due to obvious problems with their photometry. In particular, IC 10 is a very large galaxy suffering from heavy extinction and severe crowding by foreground stars. NGC 1560 was omitted because it is a late-type spiral.

To establish homogeneous distances, the absolute magnitude of the TRGB was estimated from

$$M_{I,TRGB} = (-3.935 \pm 0.028) \quad (3)$$

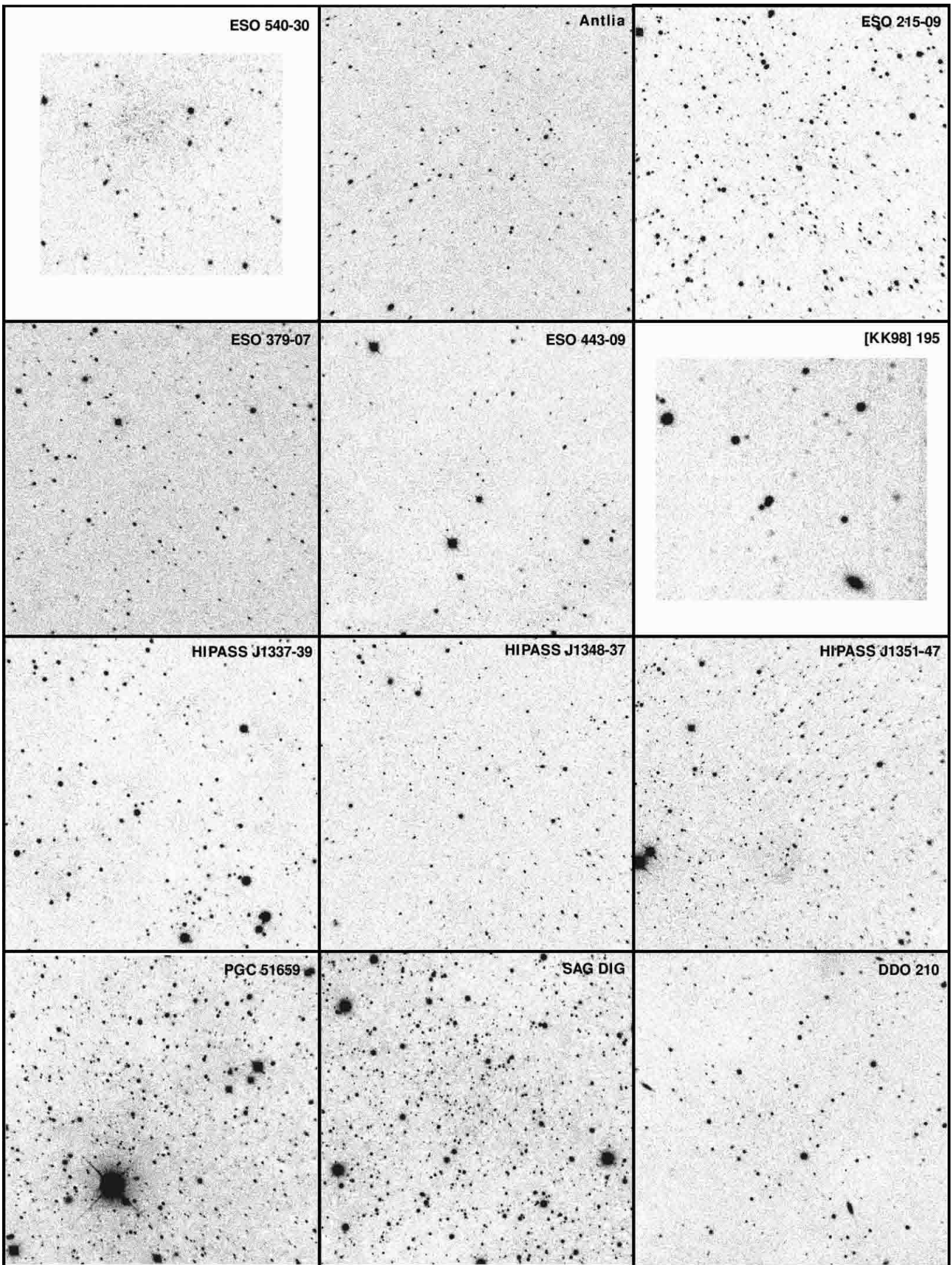


Fig. 2. Images in K_s of the fields of galaxies either marginally or not detected at CTIO (Blanco) and La Silla (NTT). North is up, and East is to the left. The fields of view are about $5' \times 5'$ (Blanco) and $2.5' \times 2.5'$ (NTT).

$$+(0.217 \pm 0.020) [(V - I)_{TRGB} - 1.6]$$

where $(V - I)_{TRGB}$ is the mean colour of the stars at the tip corrected for extinction and redshift (see Rizzi et al. 2007). The zero-point was determined from a pairwise analysis of 127 distances to 34 nearby galaxies derived from Cepheids, planetary nebulae, surface brightness fluctuations, and the TRGB (McCall, M. L., in preparation), and is anchored to the maser distance to NGC 4258 (a distance modulus of 29.29; Herrnstein et al. 1999; Gibson et al. 2000; Macri et al. 2006). The uncertainty is that due to random errors only; it does not include the uncertainty in the distance to NGC 4258. The rate of change of the absolute magnitude of the TRGB with colour was adopted from Rizzi et al. (2007).

Apparent magnitudes and colours of TRGB stars were extracted from the literature. In instances where colours were not recorded, they were estimated through inspection of colour-magnitude diagrams. Where necessary, conversion of HST photometry to the Johnson-Cousins system was accomplished using the transformation equations of Sirianni et al. (2005). Apparent magnitudes and colours were corrected for extinction and redshift (i.e., K-corrections) using the York Extinction Solver (McCall 2004). Optical depths were computed from $B - V$ colour excesses tabulated by Schlegel et al. (1998), and these were converted into extinctions and $V - I$ colour excesses assuming the spectral energy distribution of an M0 giant. The adopted reddening law was that of Fitzpatrick (1999), tuned to deliver a ratio of total-to-selective extinction of 3.07 for Vega (see McCall 2004). Colour excesses, extinctions, corrected TRGB magnitudes and colours, and the resulting distance moduli for the 66 sample galaxies are recorded in Table 3. Adopted heliocentric velocities are given in Table 4. All K-corrections were less than 0.01 mag. Uncertainties in distance moduli are estimated to be 0.10 mag typically.

This paper extends work on absolute magnitudes of dwarfs into the realm of masses, motivated by the fact that dIs and BCDs retain a large fraction of their mass in gaseous form. It is reasonable to expect that any correlation of absolute magnitude with dynamics will have scatter enhanced by variations in gas fractions, because the stellar component is often a minority of the visible mass (see Section 6.1). The determination of a baryonic mass requires that both the stellar and gaseous masses be constrained.

The mass of stars in each galaxy was judged to be most reliably signified by the luminosity in K_s , because the light from young stars is suppressed and the mass-to-light ratio is less sensitive to the star formation history than in bluer passbands (Joy & Lester 1988; Portinari et al. 2004; Vaduvescu et al. 2005). The absolute magnitude of the diffuse stellar component was determined from the integrated magnitude of the sech function modeling the two-dimensional surface brightness profile. The luminosity of any co-existing starburst was estimated by integrating the flux under the fitted Gaussian. Corrections for extinction and redshift (i.e., K-corrections) were accomplished as for the TRGB, but using the Im spectral energy distribution of McCall (2004). In computing luminosities from absolute magnitudes, the absolute magnitude of the Sun was adopted to be 3.315 in K_s (Holmberg et al. 2006; Flynn et al. 2006). Note that no corrections for redshift dimming were applied. All galaxies in the sample are at low redshift, and the entire range spanned by dimming corrections is only 0.01 mag.

Parameters describing the light distributions of the 66 sample galaxies are given in Table 4. Listed are the corrected value μ_0 of the central surface brightness in mag arcsec^{-2} , the sech scale

length r_0 converted to parsecs, the axis ratio q , the limiting radius of the surface photometry in units of r_0 , and the source of the photometry. The derived absolute magnitude M_{K_s} of the sech component and the ratio of the luminosity of any burst relative to the luminosity of the sech component are given in Table 5. The adopted value of the extinction is included in Table 3. Generally, for galaxies observed on more than one occasion, parameters describing the fit to the deepest profile are presented. However, parameters listed for ESO 381-18 and IC 4247 come from averages of fits to two independent observations.

The mass of gas was determined from the integrated flux of HI at 21 cm. Given the flux F_{HI} in K km s^{-1} , the mass M_{gas} in solar units was computed from

$$M_{gas} = k_{21} D_{Mpc}^2 F_{HI} / X \quad (4)$$

where D_{Mpc} is the distance in Mpc, X is the mass fraction of hydrogen, and $k_{21} = 2.356 \times 10^5 \text{ M}_\odot \text{K}^{-1} \text{km}^{-1} \text{s}$. The value of X was adopted to be 0.735 on the basis of measurements of the rate of change of the helium and metal fractions with the oxygen abundance in dwarfs (Izotov & Thuan 2010), presuming a mean oxygen abundance of 8.25 for the current sample and a primordial helium mass fraction of 0.257 (Izotov & Thuan 2010). For galaxies for which multiple measurements of F_{HI} were available, the single-dish measurement with the highest signal-to-noise ratio was normally adopted, unless there was evidence for confusion or peculiarities in the spectrum. The adopted fluxes and sources are listed in Table 4, and corresponding gas masses are given in Table 5.

The width of the 21 cm line at 20% of the peak, W_{20} , was used to quantify internal motions. The choice of W_{20} over the width at 50% of the peak was motivated by a desire to measure kinematics representative of the broadest possible body of gas.

Earlier studies of the fundamental plane for dIs relied upon line widths with generally poor velocity resolution. Most were taken from the Third Reference Catalogue of Bright Galaxies (de Vaucouleurs et al. 1991). For this paper, a comprehensive survey of the literature was made to pinpoint 21 cm line profiles with the highest resolution and least noise. Where 20% line widths were not recorded, they were measured from the plotted profiles or, if justifiable, established mathematically from a fit used to determine the tabulated 50% line width. Because line profiles for the galaxies in this sample were very close to being Gaussian in shape, the apparent line width W_{20}^{app} was corrected for instrumental broadening by subtracting in quadrature the width of a Gaussian instrumental profile as defined by the full-width at half-maximum R (see Verheijen & Sancisi 2001):

$$W_{20} = \frac{W_{20}^{app}}{(1+z)} \sqrt{1 - \frac{\ln 5}{\ln 2} \left(\frac{R}{W_{20}^{app}} \right)^2} \quad (5)$$

Here, R , W_{20}^{app} , and W_{20} are in km s^{-1} . The factor of $1+z$ corrects the width for redshift broadening. The adopted values of the heliocentric velocity, W_{20}^{app} , R , and $\log W_{20}$, as well as the sources of the data, are given in Table 4.

5. Analysis

5.1. Overview

Investigations below concentrate on elucidating how observed kinematics of dwarfs are tied to their scale and structure. In the process, they lead to insights on what is driving gas motions, constraints on the mass-to-light ratio of stars, an evaluation of

how close the galaxies are to being virialized, and the establishment of a method for determining reliable distances to unresolvable objects.

The most important correlations between intrinsic galaxy properties (absolute magnitude, mass, and potential) and distance-independent observables (HI line width, central surface brightness, and axis ratio) are displayed along with their fits in Figure 3. The ordinates of the panels have been configured to span identical ranges in magnitude units, so that the apparent vertical dispersions about the fits are inter-comparable. The displayed correlations are founded upon the properties of the sech component of the light profiles alone. Derived global properties of the galaxies are summarized in Table 5. The relevance of the burst component and the distribution of the properties of bursting galaxies are discussed in Section 5.5.

The correlations were defined without correcting line widths for projection. Even though it is known that some of the more massive dwarfs are rotating (e.g., Epinat et al. 2008; Swaters et al. 2009), there is considerable evidence that the kinetic energy of the gas in most of the galaxies in the sample is predominantly disordered (Vaduvescu et al. 2005, and this work). For example, line profiles tend to be Gaussian in shape, and the sensitivity of line widths to the ellipticity of isophotes is weak at best, implying that motions are close to isotropic (see Section 5.4).

All galaxies in the sample are displayed in Figure 3, but only the 48 galaxies marked by large open circles were included in fitting. Photometry originating from 2MASS becomes suspect for galaxies whose surface brightnesses are as low as is typical of sample members (Kirby et al. 2008), and galaxies whose surface brightness profiles do not extend beyond 2.5 sech scale lengths tend to display deviant properties. Consequently, the following galaxies were excluded from the fits:

- four dwarfs observed by 2MASS only (Ho II, NGC 3077, NGC 4214, and NGC 6822, marked by crosses)
- in addition to two of the 2MASS galaxies (Ho II and NGC 6822), six dwarfs for which photometry did not extend beyond $2.5r_0$ (Cam B, ESO444-84, KK98 230, KKH 86, Peg DIG, and UGCA 92, marked by solid circles)
- one object which displays a spiral-like morphology in HI and whose surface brightness profile is convex in the core (NGC 2915)
- seven extreme deviants identified during the course of analysis (DDO 47, DDO 168, ESO215-09, ESO223-09, KK98 17, KK98 182, and UGC 3755), all of which are signified by small open circles

The last seven galaxies were revealed by a large gap in the histogram of residuals for the fit to the potential versus line width and surface brightness. They lie 3.1σ or more away from the fit, whereas the most extreme of the retained galaxies lie within 1.8σ of that fit.

For maximum flexibility, fits were determined using the downhill simplex algorithm (Nelder & Mead 1965; Press et al. 1986). For certain fits involving the stellar mass, it was postulated that any fundamental relationship is one for which there exists a mass-to-light ratio which minimizes the dispersion. Stable solutions to the mass-to-light ratio proved to be possible by combining the simplex algorithm with a golden section search.

Uncertainties in derived parameters were ascertained through Monte Carlo simulations. The starting point for these simulations were estimates for typical errors in the observables. The adopted uncertainties were 0.1 mag for distance moduli, 0.15 mag for μ_0 , 5% for r_0 , 10% for q , 0.23 mag for m_{sech} , 5% for

W_{20} , and 10% for F_{HI} . In each analysis, 1000 random deviates of these observational quantities were computed, from which deviates for the derived quantities were computed and fitted. Below, any quoted uncertainty in a fitted parameter is the average of the standard deviations of the resulting solutions on either side of the solution obtained from the reference fit.

5.2. Absolute magnitude

The upper left panel of Figure 3 displays the Tully-Fisher relation for the dwarfs, albeit with no correction of line widths for tilt (as discussed above). As expected, the dispersion is large. The fitted relation is

$$M_{K_s, sech} = (-16.424 \pm 0.040) - (5.066 \pm 0.207)(\log W_{20} - 1.8) \quad (6)$$

with the standard deviation being 0.95 mag. By comparison, the expected vertical scatter due to observational errors alone is only 0.27 mag (the quadrature sum of the uncertainties in the abscissa and ordinate). Even if all motions were rotational, the dispersion in axis ratios is such that only about 0.5 mag of the scatter would be attributable to projection.

The upper right panel of Figure 3 displays the fundamental plane of Vaduvescu et al. (2005), with the fit updated. For the sample here,

$$M_{K_s, sech} = (-16.490 \pm 0.041) - (2.789 \pm 0.243)(\log W_{20} - 1.8) + (0.721 \pm 0.043)(\mu_0 - 20) \quad (7)$$

where μ_0 is the *observed* central surface brightness in mag arcsec⁻² (i.e., without any correction for projection). The standard deviation is 0.63 mag. The dispersion worsened when surface brightnesses were corrected for tilt (assuming an oblate spheroidal geometry: see Section 5.4). Efforts to improve the fit by attributing some of the motions to rotation, and correcting for tilt accordingly, met with failure. The scatter is larger than suggested by Vaduvescu & McCall (2008), probably because of changes to rejection criteria. Most importantly, as noted by Vaduvescu & McCall (2008), it is much larger than the dispersion to be expected on the basis of observational errors alone, which is 0.28 mag.

5.3. Mass

The unexplained scatter in absolute magnitudes motivated the development of a corresponding plane for the baryonic mass M_{bary} which would accommodate the often significant but highly variable proportion of matter in gaseous form. There was reason to be optimistic that a well-defined relationship might be found because the baryonic Tully-Fisher relation for rotationally-supported systems is so tight (McGaugh et al. 2000; McGaugh 2005, 2011). Most of the galaxies in the sample appear to be pressure-supported, with random motions being close to isotropic (see Section 5.4), so on energy grounds it is reasonable to construct the baryonic Tully-Fisher relation by substituting radial velocity dispersions for circular velocities (McGaugh et al. 2010; Wolf et al. 2010).

The computation of baryonic masses required the adoption of a mass-to-light ratio for the stars, since

$$M_{bary} = \Upsilon L_{K_s} + M_{gas} \quad (8)$$

Here, L_{K_s} is the luminosity in K_s and $\Upsilon = M_{stars}/L_{K_s}$ is the mass-to-light ratio of the stars in K_s . Attention was restricted to

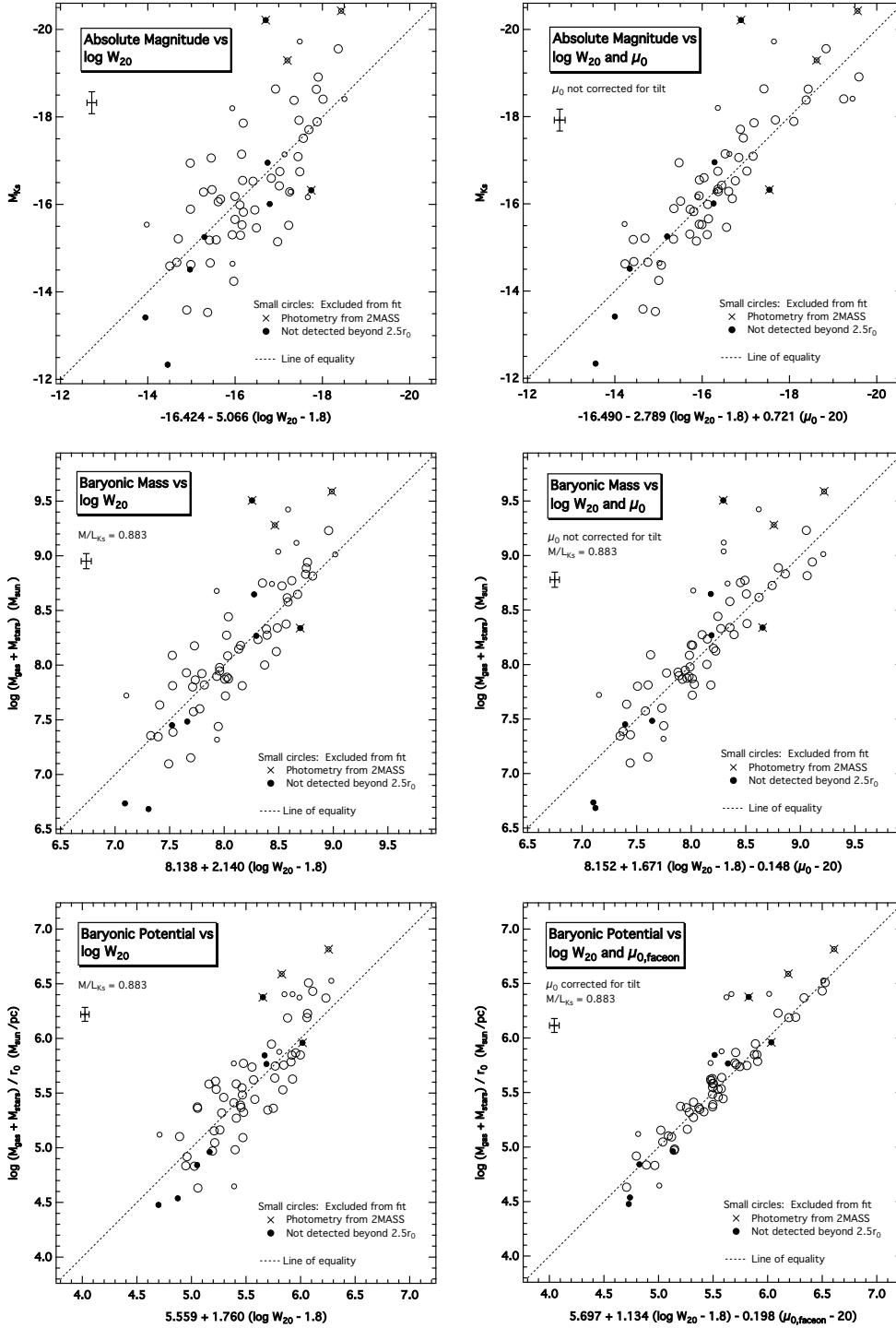


Fig. 3. Correlations among intrinsic and observed properties of star-forming dwarfs. In all panels, line widths have been corrected for resolution but not for tilt. In magnitude units, the range of ordinates is the same for all panels, so vertical dispersions are directly comparable. Typical uncertainties in abscissae and ordinates are depicted by an error cross in the upper left corner of each panel. *Top left:* Absolute magnitude in K_s versus the HI line width (the Tully-Fisher relation); *Top right:* Absolute magnitude in K_s versus the HI line width and the observed central surface brightness (the *dI fundamental plane* of Vaduvescu et al. 2005, with an updated fit). Correcting the surface brightnesses for tilt worsens the fit; *Middle left:* Baryonic mass versus the HI line width, based upon a mass-to-light ratio in K_s derived from the fit to the potential plane; *Middle right:* Baryonic mass versus the HI line width and the observed central surface brightness, based upon a mass-to-light ratio in K_s derived from the fit to the potential plane. Correcting the surface brightnesses for tilt does not improve the fit; *Bottom left:* Baryonic potential versus the HI line width, based upon a mass-to-light ratio in K_s derived from the fit to the potential plane; *Bottom right:* Baryonic potential versus the HI line width and tilt-corrected central surface brightness (the *potential plane*), based upon a mass-to-light ratio in K_s derived during the fitting. In all panels, every galaxy in the sample is plotted, but only galaxies marked with large circles were fitted. Excluded from the fits were four galaxies observed exclusively by 2MASS (crosses), six galaxies in addition to two 2MASS galaxies for which photometry did not extend beyond 2.5 sech scale lengths (solid circles), one galaxy with an unusual morphology (small open circle), and seven extreme outliers identified while fitting the potential (small open circles).

the sech component of the light distribution. The contribution of a burst component to the mass was assumed to be negligible. This approximation is justified in Section 5.5, where the consequences of accommodating the light of a burst are discussed.

The best estimate of Υ was gained from analysis of the gravitational potential (see Section 5.4), which yielded a solution of 0.88 ± 0.20 . To establish the most credible relationship between the baryonic mass and observables, then, the mass-to-light ratio was fixed at 0.88. The corresponding stellar and baryonic masses are summarized in Table 5.

Surprisingly, the baryonic Tully-Fisher relation proved to be as highly dispersed as the fundamental plane. It is displayed in the middle left panel of Figure 3. The fitted relation is given by

$$\log M_{\text{bary}} = (8.138 \pm 0.012) + (2.140 \pm 0.064)(\log W_{20} - 1.8) \quad (9)$$

The dispersion is 0.24 dex (0.61 mag), versus the expected value of 0.08 dex based upon observational uncertainties alone.

An improvement to the baryonic Tully-Fisher relation was realized by introducing surface brightness as a second parameter. The resulting baryonic plane, which is displayed in the middle right panel of Figure 3, is described by

$$\log M_{\text{bary}} = (8.152 \pm 0.012) + (1.671 \pm 0.074)(\log W_{20} - 1.8) + (-0.148 \pm 0.013)(\mu_0 - 20) \quad (10)$$

(for $\Upsilon = 0.88$). The standard deviation is 0.20 dex (0.49 mag). Although lower than found for the Tully-Fisher relation, it is still much higher than the expected value of 0.08 dex based upon observational uncertainties. The fit did not improve when the surface brightnesses were corrected for projection (see Section 5.4). Allowing Υ to be free, the dispersion dropped somewhat to 0.17 dex. However, the solution for Υ was 0.15 ± 0.05 , which is unreasonably low compared to expectations from population syntheses (Portinari et al. 2004).

5.4. Potential

Thirty-two galaxies in the sample have line profiles which have been observed with a resolution of 2 km s^{-1} or less. Profiles are close to being Gaussian in shape, which suggests that the dynamics of dIs may be simple. As a starting point, it is reasonable to posit that the systems are close to being virialized. Virialization requires that

$$2T + \Omega = 0 \quad (11)$$

where T is the kinetic energy and Ω is the potential energy. If the line width is predominantly controlled by gravity, and if the potential defined by the baryonic mass scales with the potential setting the line width (which in large part must be controlled by the amount of dark matter), then one might surmise that

$$P \equiv M_{\text{bary}}/r_0 \propto (W_{20})^2 \quad (12)$$

Henceforth, P will be referred to as the ‘‘baryonic potential’’.

The baryonic potential (the stellar component of which being defined by the mass of the sech component) is plotted as a function of line width in the lower left panel of Figure 3. The relationship is given by

$$\log P = (5.559 \pm 0.011) + (1.760 \pm 0.058)(\log W_{20} - 1.8) \quad (13)$$

The standard deviation of the fit is 0.24 dex (0.59 mag), which, surprisingly, is comparable to that for the fits to the baryonic mass. However, the introduction of surface brightness as a second parameter reduced the dispersion drastically. With the mass-to-light ratio fixed at 0.88 (see below), the following relationship was found:

$$\log P = (5.578 \pm 0.011) + (1.101 \pm 0.065)(\log W_{20} - 1.8) + (-0.208 \pm 0.012)(\mu_0 - 20) \quad (14)$$

The standard deviation is only 0.12 dex (0.29 mag). The dispersion did not change significantly when the mass-to-light ratio was allowed to vary.

Figure 4 shows the residuals in the fit to the potential as a function of the logarithm of the axis ratio q . Residuals become more negative as galaxies flatten. To a significant extent, this is likely to be a consequence of the effect of projection on surface brightnesses. For an oblate spheroid, the surface brightness varies with q as

$$\mu_0 = \mu_0^{i=0} + 2.5 \log q \quad (15)$$

where $\mu_0^{i=0}$ is the surface brightness that would be measured if the view were face-on (inclination i equal to zero). The dashed line in Figure 4 displays the rate at which residuals in the potential should vary with q if surface brightnesses are affected by projection in the way expected for oblate spheroids. The observed trend is very close to that predicted. Thus, a further refinement to the fit to the potential was possible by correcting surface brightnesses to a common viewing angle (face-on).

It was unclear how line widths dominated by random motions might vary with tilt. For the purpose of investigation, any sensitivity to tilt was approximated as a power law in q . Then, to convert measurements to face-on,

$$W_{20}^{i=0} = q^\gamma W_{20} \quad (16)$$

where γ is a constant. It was expected that a relationship between the potential, line width, and surface brightness which is free of projection effects would have the form

$$\log P = a + b \log q^\gamma W_{20} + c(\mu_0 - 2.5 \log q) \quad (17)$$

$$= a + b \log W_{20} + c\mu_0 + (\gamma b - 2.5c) \log q \quad (18)$$

where a , b , and c are constants. By introducing $\log q$ as a third variable, it was possible to constrain γ .

With Υ fixed at 0.88, and with the geometry approximated to be oblate spheroidal, the solution for γ was -0.10 . The sign is opposite to what would be expected if flattening is a consequence of anisotropic motions, be they ordered or disordered. Also, $|\gamma|$ is small, suggesting that motions are close to being isotropic. It was concluded that the trend in the residuals of the potential with the axis ratio should be attributed primarily to variations in surface brightness expected for oblate spheroids viewed at different angles.

In the end, given how weakly line widths appeared to depend on tilt and uncertainty about precisely how they did, only surface brightnesses were corrected for projection. The relationship between the potential, apparent line width, and the surface brightness corrected to face-on (via Equation 15) is displayed in the lower right panel of Figure 3. With the mass-to-light ratio free to vary, the fit was given by

$$\log P = (5.697 \pm 0.065) + (1.134 \pm 0.080)(\log W_{20} - 1.8) + (-0.198 \pm 0.018)(\mu_0^{i=0} - 20) \quad (19)$$

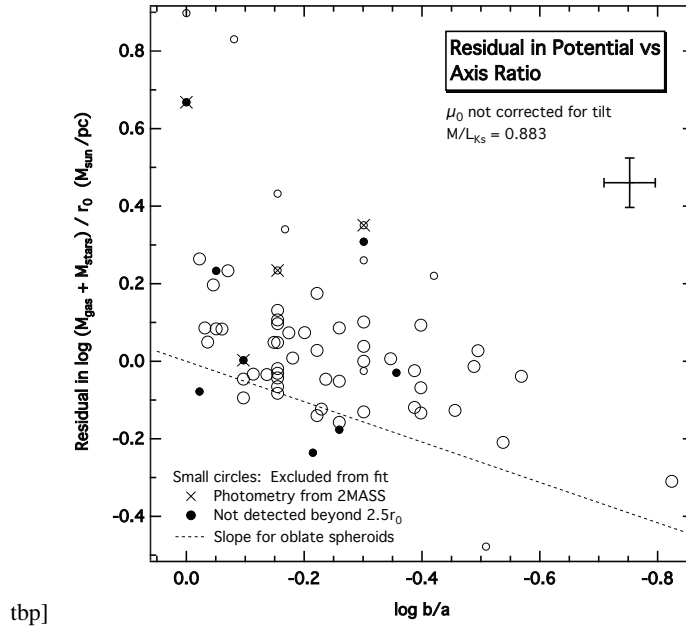


Fig. 4. Residuals in the potential as a function of the axis ratio $q = b/a$. The dashed line displays the slope of the expected relationship for oblate spheroids (the y-intercept having been fixed at zero).

The corresponding solution for Υ was 0.883 ± 0.199 . Resulting values of $\log M_{stars}$, $\log M_{bary}$, and $\log P$ are listed in Table 5. Uncertainties in the coefficients are higher than for Equation 14 because of the freedom in the mass-to-light ratio. The standard deviation is only 0.096 dex (0.24 mag). The vertical dispersion expected from random observational errors is 0.08 dex. Thus, a structural relationship has been identified for dwarfs for which observational errors overwhelm the cosmic dispersion. This relationship can be regarded as a *more* fundamental plane for dwarfs, and henceforth will be referred to as the *potential plane*.

Although the solution for the mass-to-light ratio is twice as high as measured for the disk of the Milky Way from vertical kinematics (Portinari et al. 2009), it is nevertheless compatible with syntheses of exponential disks spanning a range of possible star formation histories (Portinari et al. 2004). It should be noted, though, that the estimate for Υ is in part a dynamical estimate of the mass-to-light ratio, since it is tied to line widths. The tightness of the correlation lends credence to the postulate that the mass and size of dark matter haloes scale straightforwardly with the mass and distribution of luminous matter.

To check the sensitivity of the fit to the selection of galaxies, random subsets of the original galaxy sample were formed by removing 10% of the objects (5 galaxies). A total of 100 subsets were constructed and fitted. The mean values of the free parameters agreed extremely well with those determined from the entire sample. Most important, the mean value of Υ was 0.895 ± 0.095 , which is almost identical to the value derived by fitting the whole sample. Because observational errors are predominant in setting the dispersion, it is not believed that the solution for the mass-to-light ratio suffers from biases which plague fits to less fundamental relations.

5.5. Blue compact dwarfs and turbulence

Despite much research, the relationship between dIs and BCDs is not clear yet. Structurally, they appear to be similar, because the near-infrared light profile of a BCD can be modeled well by superimposing a Gaussian starburst upon a sech function

(Vaduvescu et al. 2006). Thus, it is reasonable to consider any star-forming dwarf to be a blue compact dwarf if its light profile in K_s displays an excess of light in the core over what is expected for a pure sech law. That is the definition adopted here.

The left panel of Figure 5 re-displays the correlation of the potential with line width and face-on central surface brightness (Equation 19). Those galaxies with an excess of light in the core, i.e., the BCDs, are marked with solid circles, and normal dIs are marked with open circles. Starbursts span the entire range of galaxies in the sample. Fits to the pure sech dwarfs and the BCDs separately were consistent within errors, proving that there is no segregation. It appears that gravity, not turbulence, is the predominant determinant of gas kinematics in most of the star-forming dwarfs in the sample. The mere existence of strong correlations of the baryonic mass and the potential with line width lends support to this conclusion. Also, the dependence of the potential on surface brightness is opposite to what would be expected if line widths were inflated by gas flows stemming from recent star formation. For a gas-dominated system at least, any concomitant enhancement in surface brightness would be expected to be incorporated in such a way as to oppose the change in line width and thereby preserve the potential. Instead, the sign of the coefficient of $\mu_0^{i=0}$ in Equation 19 is such that brightening and broadening change the potential in the same way.

To examine the influence of the Gaussian component on the fit to the potential, the mass-to-light ratio of stars in the burst relative to the mass-to-light ratio of stars in the sech was introduced as a free parameter. Then, luminosities of both the burst and sech components were employed to compute baryonic masses. The solution for the ratio of mass-to-light ratios was zero, meaning that the inclusion of a non-negligible burst mass degrades the correlation. However, forcing the ratio of mass-to-light ratios to unity led to a fit which was still reasonable. A larger sample of BCDs in which the burst light is a significant fraction of the total light will be required to constrain more reliably the appropriate mass-to-light ratio to use to accommodate the burst mass in the definition of the potential.

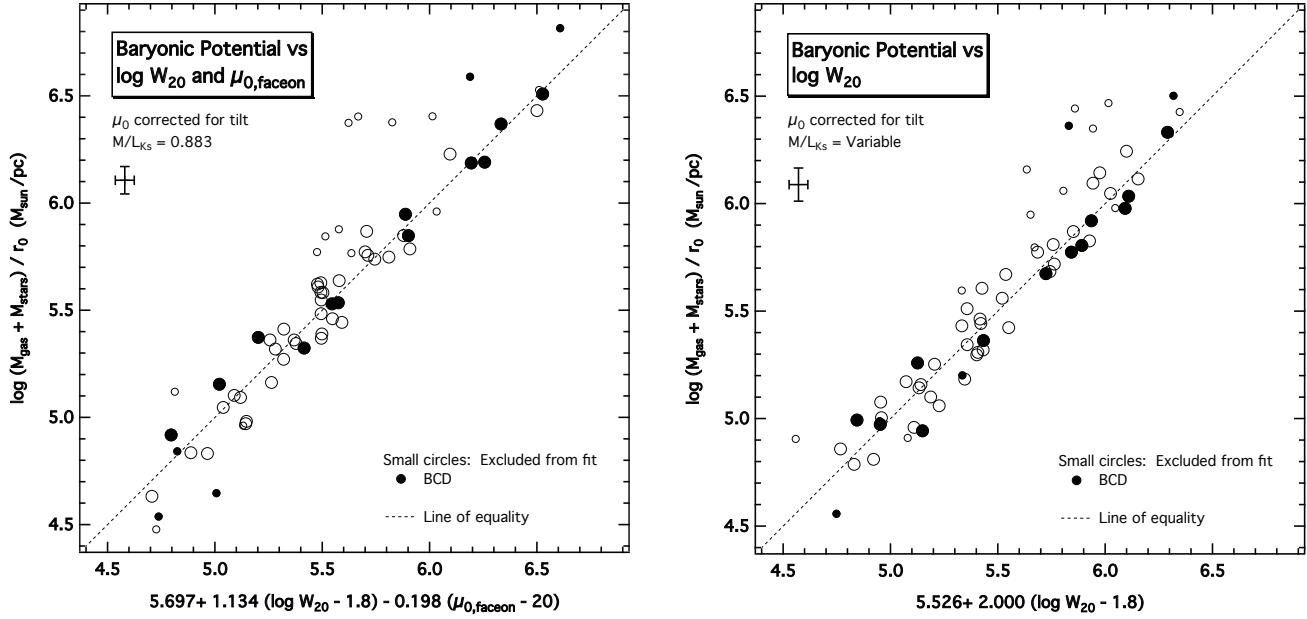


Fig. 5. Two renditions of the potential for dwarfs. *Left:* M_{stars}/L_{Ks} fixed. *Right:* M_{stars}/L_{Ks} variable. Individualized mass-to-light ratios for the plot on the right were estimated from the amount by which the central surface brightness of the sech component deviated from the mean for a given line width under the condition that the galaxies are virialized (see Figure 6). In both panels, dwarf irregulars (dIs) are marked with open circles, and blue compact dwarfs (BCDs) are flagged by solid circles. No matter how the mass-to-light ratios are computed, BCDs and dIs populate the diagrams in the same way.

6. Discussion

6.1. Variable mass-to-light ratios and virialization

Equation 19 reveals that

$$P \propto [W_{20}]^{1.13} [I_0^{i=0}]^{0.49} \quad (20)$$

where $I_0^{i=0}$ is the face-on central surface brightness of the sech model in linear units. Although the virial theorem motivated the quest for this relation, the exponent of W_{20} is half what it should be. The dependence on the surface brightness is puzzling, too. Possibly, it is a reaction to variations in the mass-to-light ratio. A dwarf which has undergone star formation more recently than is typical for galaxies of its kind in the sample may show enhancements in both surface brightness and luminosity relative to the norm for its potential. If so, the mass-to-light ratio ought to be reduced by a factor which preserves the value of the potential. In effect, such a reduction is happening through the dependence of P on $I_0^{i=0}$, although it is complicated by the presence of gas. It is even possible that, in not accounting for variability in Υ , the true dependence of the potential on the line width is obscured.

To individualize mass-to-light ratios, and thereby assess the impact on the relationship between the potential and internal motions, the premise was made that any deviation of the surface brightness from the mean at a given line width is a consequence of a different star formation history, and that the deviation is simultaneously incorporated in the luminosity of stars associated with the sech component. Then, the mass-to-light ratio Υ relative to some reference value Υ_{ref} could be estimated from the face-on central surface brightness $\mu_0^{i=0}$ relative to an appropriate norm $\mu_{0,ref}^{i=0}$ as follows:

$$\log(\Upsilon/\Upsilon_{ref}) = 0.4(\mu_0^{i=0} - \mu_{0,ref}^{i=0}) \quad (21)$$

In principle, the mean surface brightness $\mu_{0,ref}^{i=0}$ could be tied to global properties. Figure 6 reveals the correlation of $\mu_0^{i=0}$ with $\log W_{20}$. There is a tendency for surface brightnesses to brighten with the line width, although the scatter is large. The correlation must in part be responsible for weakening the W_{20} -dependence of the potential relative to what is expected for virialized systems.

If it is hypothesized that star-forming dwarfs really are virialized, it is possible to predict how rapidly $\mu_{0,ref}^{i=0}$ must vary with $\log W_{20}$, and thereby test compatibility with the observations. To this end, it was approximated that $\mu_{0,ref}^{i=0}$ varies linearly with $\log W_{20}$. Based upon the earlier fit to the potential with Υ held fixed, it was reasonable to approximate Υ_{ref} to be 0.883. Noting that Υ for each dwarf is defined by Equation 21, it was possible to solve for the coefficients of the relation between $\mu_{0,ref}^{i=0}$ and $\log W_{20}$ by minimizing the dispersion in the relationship between the potential and $\log W_{20}$.

The dashed line in Figure 6 displays the solution for the correlation between $\mu_{0,ref}^{i=0}$ and $\log W_{20}$ which arose when the galaxies were required to be virialized. It is defined by

$$\mu_{0,ref}^{i=0} = (20.778 \pm 0.214) + (-4.371 \pm 0.296)(\log W_{20} - 1.8) \quad (22)$$

The data admit the possibility of such a trend. The right panel of Figure 5 shows the simultaneous fit to the potential, with baryonic masses now determined using individualized mass-to-light ratios computed from Equations 21 and 22 (with Υ_{ref} set to 0.883). It is described by

$$\log P = (5.526 \pm 0.041) + 2(\log W_{20} - 1.8) \quad (23)$$

Of course, the coefficient in front of $\log W_{20}$ was forced by the requirement that the systems be virialized. The standard deviation about the fit is 0.105 dex (0.26 mag), which is only a little worse than that for the potential plane (Equation 19).

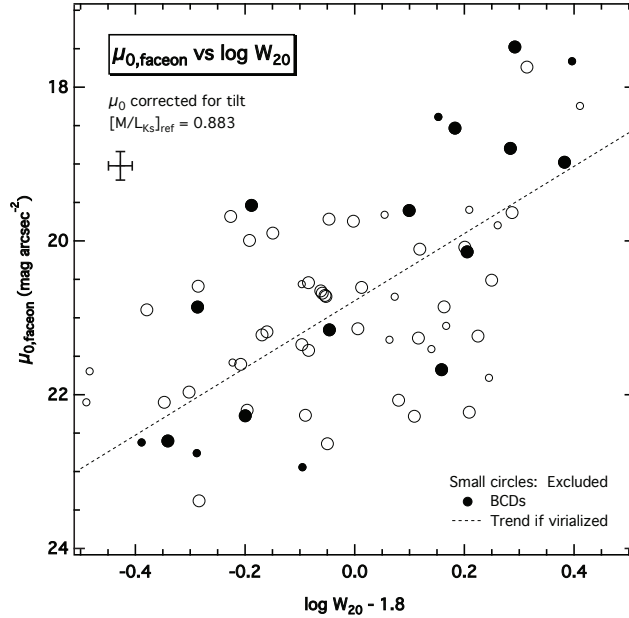


Fig. 6. Tilt-corrected central surface brightness of the sech component as a function of the HI line width. Dwarf irregulars (dIs) are marked with open circles, and blue compact dwarfs (BCDs) are flagged by solid circles. The dashed line is the required relationship if the galaxies are virialized, based upon a reference mass-to-light ratio of 0.883.

Resulting mass-to-light ratios are listed in Table 5 and displayed as a function of $\log W_{20}$ in Figure 7. The range of variation is fairly large, in many cases beyond what is reasonable to expect in K_s for typical star formation histories (Portinari et al. 2004). Observational errors are in part to blame, since mass-to-light ratios vary to compensate for errors in surface brightness.

Figure 8 compares the gas fractions computed from a fixed value of the mass-to-light ratio ($\Upsilon = 0.88$) with the gas fractions derived when the mass-to-light ratio is allowed to vary as above. The spread in gas fractions at large W_{20} is reduced when variable mass-to-light ratios are employed. For many starbursting dwarfs, the gas fraction rises. This is because surface brightnesses for these galaxies are unusually high, leading to downward adjustments to mass-to-light ratios and consequent reductions in the stellar masses. Gas fractions for many dwarf irregulars also change significantly, rising for the least massive galaxies and declining for the most massive.

6.2. Distances

The discovery of tight correlations between the gravitational potential and distance-independent observables opens up a way of mapping the spatial distribution of dwarf galaxies on large scales. Locally, dwarfs are more dispersed than giants, so the relationship offers an avenue for exploring the distribution of matter in mass-poor regions of the universe. A huge advantage over the Tully-Fisher relation for spirals is that no restriction need be placed on tilt. In fact, the method for correcting surface brightness for the viewing angle does not even require that the tilt be evaluated (a complicated problem owing to the possible variability of the intrinsic axis ratio).

For any galaxy, the value of $P \equiv M_{\text{bary}}/r_0$ in $M_{\odot} \text{pc}^{-1}$ can be estimated from observations of the 21 cm line width $\log W_{20}$, the central surface brightness μ_0 , and the axis ratio q using Equation 19 or 23. This provides an avenue to determining the distance. Define m_{sech} to be the apparent magnitude of the sech component of the light distribution corrected for extinction and

redshift, $r_{0, \text{arcsec}}$ the sech scale length in arc seconds, Υ the mass-to-light ratio in solar units for the stars constituting the sech component (for the passband defining m_{sech}), F_{21} the 21 cm line flux in K km s^{-1} , X the fraction of the gas mass which is hydrogen, and k_{21} the factor required to convert the HI line flux to hydrogen mass. The distance modulus D_{mod} is given by

$$D_{\text{mod}}/5 = \log P + \log r_{0, \text{arcsec}} - \log \left[\Upsilon 10^{-0.4(m_{\text{sech}} - M_{\odot} - 12.5)} + 10^{-5} k_{21} F_{21}/X \right] - \log(0.648/\pi) \quad (24)$$

where M_{\odot} is the absolute magnitude of the Sun (3.315 in K_s) and k_{21} has the value specified for Equation 4. For K_s , the mass-to-light ratio is either fixed at 0.883 if Equation 19 is used to estimate P , or computed from Equations 21 and 22 if Equation 23 is employed to get P (with Υ_{ref} set to 0.883).

Figure 9 shows for the galaxies defining the potential plane how the distances derived from Equation 24 compare with those derived from the TRGB. Typical uncertainties in observational quantities were given in Section 5.1. Because observational errors are responsible for the bulk of the dispersion in the potential, it is reasonable to examine the accuracy with which a distance can be determined considering observational errors alone. Based upon the uncertainties in W_{20} , μ_0 , and q , $\log P$ can be estimated to an accuracy of about 0.04 dex (Equation 19) if the cosmic dispersion is smaller. Accounting for the errors in m_{sech} , $r_{0, \text{arcsec}}$ and F_{21} , then the uncertainty in the derived distance modulus comes out to be 0.38 mag for $\Upsilon = 0.88$.

The most important contributors to the uncertainty are the errors in m_{sech} and μ_0 . In the sample studied here, these errors were quite large due to limitations in the field of view, which restricted the number of 2MASS stars available to calibrate the photometry. Significant improvements are possible using more modern detectors with wider fields of view. If the uncertainty in m_{sech} can be reduced to 0.10 mag and the uncertainty in μ_0 to 0.05 mag, then the error in the distance modulus will come down to 0.26 mag. A further reduction is possible with deeper

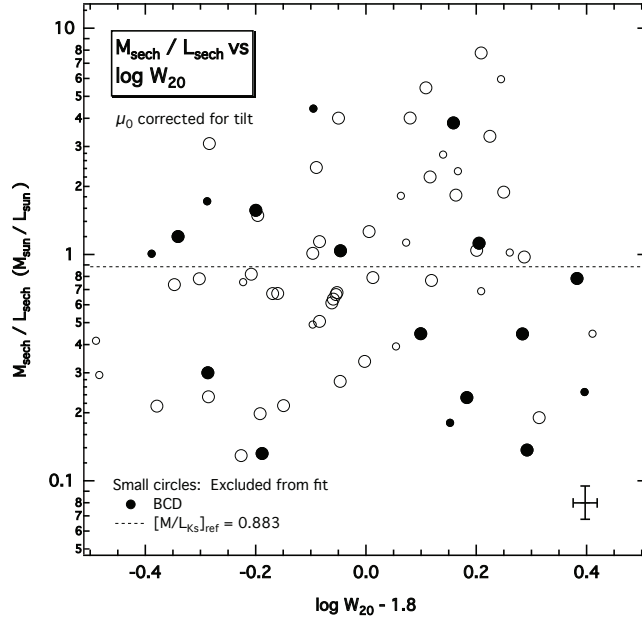


Fig. 7. Mass-to-light ratio of the sech component as a function of line width. Dwarf irregulars (dIs) are marked with open circles, and blue compact dwarfs (BCDs) are flagged by solid circles. Individualized mass-to-light ratios were determined from the deviations in surface brightness from the norms expected for virialized systems. The horizontal dashed line is the value of the mass-to-light ratio which was computed for the entire sample in establishing the potential plane of Figure 3.

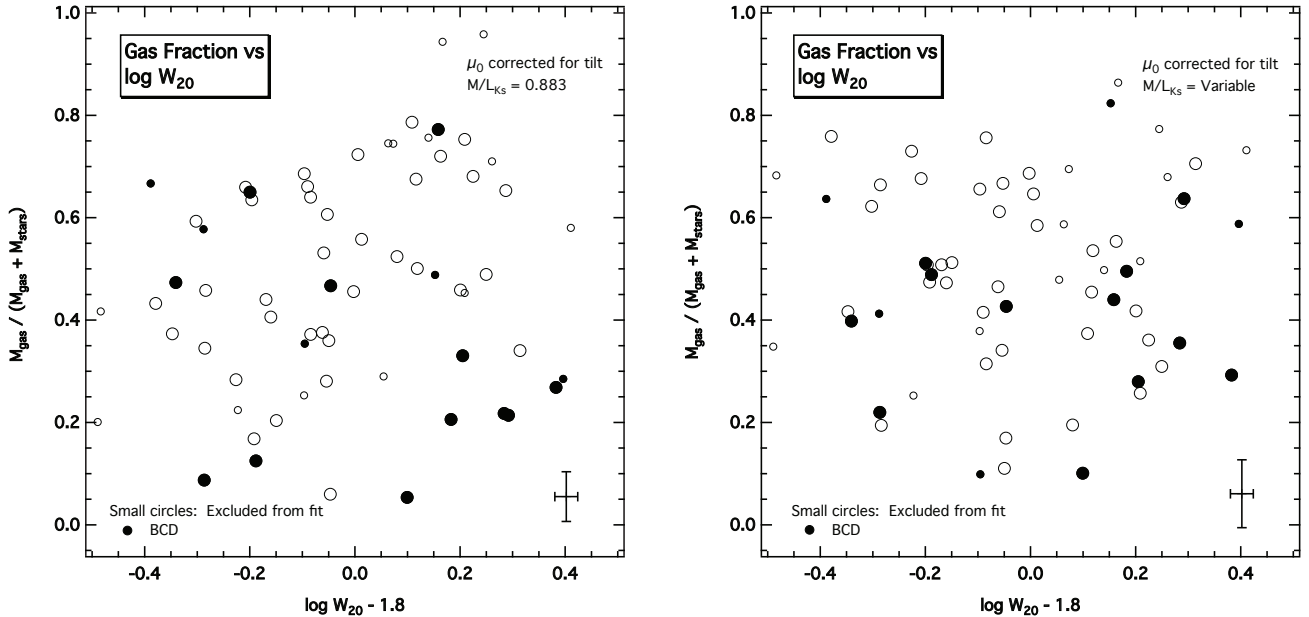


Fig. 8. Gas fractions as a function of line width. *Left:* M_{stars}/L_{K_s} fixed. *Right:* M_{stars}/L_{K_s} variable. In both panels, dwarf irregulars (dIs) are marked with open circles, and blue compact dwarfs (BCDs) are flagged by solid circles. With mass-to-light ratios adjusted for surface brightness deviations, gas fractions for many galaxies change significantly.

photometry, which would enable improvement in the accuracy with which r_0 and q are measured. Overall, it appears that the potential plane for dwarfs offers a means to determine distances to dwarfs as good as the Tully-Fisher relation yields for spirals.

7. Conclusions

Deep imaging in K_s has been presented for 19 star-forming dwarf galaxies. Structural properties were measured by fitting a sech function to surface brightness profiles, and additionally a

Gaussian for those objects displaying evidence for a central starburst (interpreted thereby as being blue compact dwarfs). Results for these galaxies were combined with photometry for others published previously to examine how kinematics, as conveyed by HI line widths, are connected to global properties.

Most dwarfs in the sample displayed HI line profiles close to Gaussian in shape. Also, in optimizing relationships among global properties and kinematics, no strong tie between apparent line widths and isophotal axis ratios was evident. Thus, in the majority of sample galaxies, most of the kinetic energy of the

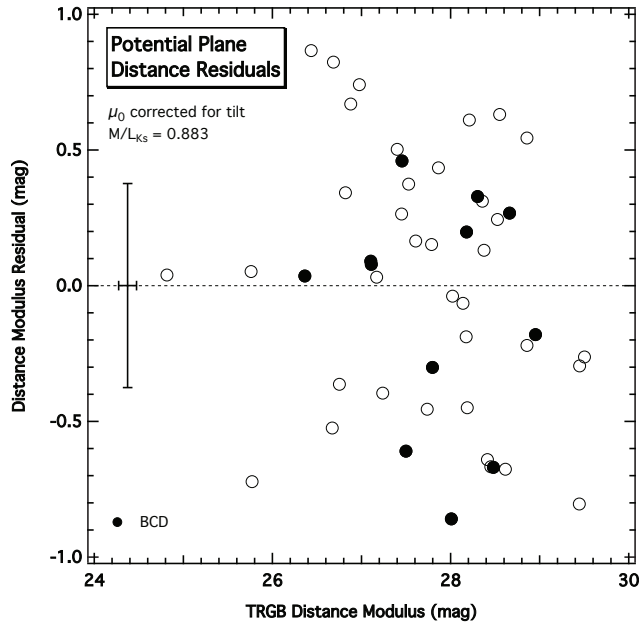


Fig. 9. Difference between the potential plane distance modulus and TRGB distance modulus as a function of the TRGB distance modulus for dwarfs defining the potential plane. The horizontal dashed line marks perfect agreement. Dwarf irregulars (dIs) are marked with open circles, and blue compact dwarfs (BCDs) are flagged by solid circles. The vertical component of the error bar shows the mean uncertainty expected for potential plane distances from observational errors if the cosmic scatter about the potential plane is zero.

gas appeared to be disordered, and internal motions appeared to be close to isotropic. Consequently, it proved to be possible to establish relationships without correcting line widths for tilt.

It was confirmed that much of the scatter in the Tully-Fisher relation for dwarfs is correlated with surface brightness. The “fundamental plane” defined by the correlation of absolute magnitude with line width and surface brightness still displayed a dispersion which exceeded what was expected from observational errors alone. Conjecturing that some of the scatter might be a consequence of not accommodating the highly variable gaseous component, the baryonic Tully-Fisher relation was constructed. It proved to be as dispersed as the fundamental plane, although some improvement was possible by adding surface brightness as a second parameter.

Motivated by the possibility that the galaxies may be virialized, the correlation between the potential and the line width was examined. The potential defined by the ratio of the baryonic mass to the sech scale length was hypothesized to be proportional to the potential setting internal motions, but the mass-to-light ratio required to compute the stellar component of the mass was left as a free parameter. The derived relationship between the potential and the line width displayed large residuals correlated with surface brightness. When surface brightness variations were accommodated, an extremely tight relationship between the potential, line width, and surface brightness resulted. Remaining residuals were found to correlate with tilt, with the bulk of the trend explainable by variations in surface brightness arising from viewing oblate spheroids at different angles. Once surface brightnesses were corrected for tilt, the remaining dispersion of this *more* fundamental plane, referred to as the *potential plane*, could be almost entirely attributable to observational errors. The solution for the mean mass-to-light ratio for the stars (i.e., the sech component of the light distribution) was 0.88 ± 0.20 . BCDs lay precisely in the plane described by dIs. The placement of BCDs, the strength of the correlation, and the

direction of the sensitivity to surface brightness all point to gravity, not turbulence, being primarily responsible for determining gas motions in star-forming dwarfs. The potential plane suggests a strong linkage between the mass and distribution of luminous matter and the mass and scale of dark matter haloes. It also offers a new avenue for determining the distances to unresolvable star-forming dwarfs which may be as good as the Tully-Fisher relation for spirals.

The potential plane described a potential varying as $W_{20}^{1.13}$, i.e., less steeply than expected for virialized systems (for which the exponent should be 2). However, the dependence of the potential on surface brightness was such that surface brightness might be considered to be acting as a proxy for variations in the mass-to-light ratio of stars. To explore this possibility, it was hypothesized that star-forming dwarfs are in fact virialized, and the required dependence of mean surface brightness on line width was derived. Deviations in surface brightness from the norm for a particular line width were used to adjust mass-to-light ratios to compensate for differing star formation histories (and observational errors). Residuals in the correlation of the modified potential with line width were only slightly degraded with respect to those for the potential plane. Computed mass-to-light ratios covered a range greater than expected from theoretical expectations, but some of the variation was attributable to the uncertainties in surface brightnesses. Further studies of star formation rates would be productive in evaluating whether the predicted range of mass-to-light ratios is justified. Work is in progress to evaluate implications for chemical evolution.

Acknowledgements. MLM is grateful to M. De Robertis for advice on testing the robustness of the fit to the potential plane, and to the Natural Sciences and Engineering Council of Canada for its continuing support. OV, EUS, MA, FPN and ABD acknowledge the Chilean TACs for the time allocation at ESO (Run ID: 081.B-0386(A)) and CTIO (2008A-0913 and 2008B-0909). This research has made use of the NASA/IPAC Extragalactic Database (NED) which is operated by the Jet Propulsion Laboratory, California Institute of Technology, under contract with the National Aeronautics and Space Administration. We acknowledge the

usage of the HyperLeda database (<http://leda.univ-lyon1.fr> - Paturel et al. 2003). Our work used IRAF, a software package distributed by the National Optical Astronomy Observatory, which is operated by the Association of Universities for Research in Astronomy (AURA) under cooperative agreement with the National Science Foundation. This research has made use of SAOImage DS9, developed by the Smithsonian Astrophysical Observatory.

References

- Banks, G. D., Disney, M. J., Knezak, P. M., et al. 1999, *ApJ*, 524, 612
 Barnes, D. G., & de Blok, W. J. G. 2004, *MNRAS*, 351, 333
 Beaulieu, S. F., Freeman, K. C., Carignan, C., Lockman, F. J., & Jerjen, H. 2006, *AJ*, 131, 325
 Begum, A., Chengalur, J. N., & Hopp, U. 2003, *New A*, 8, 267
 Begum, A., Chengalur, J. N., Karachentsev, I. D., Kaisin, S. S., & Sharina, M. E. 2006, *MNRAS*, 365, 1220
 Begum, A., Chengalur, J. N., Karachentsev, I. D., Sharina, M. E., & Kaisin, S. S. 2008, *MNRAS*, 386, 1667
 Bureau, M., & Carignan, C. 2002, *AJ*, 123, 1316
 Cote, S., Freeman, K. C., Carignan, C., & Quinn, P. J. 1997, *AJ*, 114, 1313
 Dalcanton, J. J., Williams, B. F., Seth, A. C., et al. 2009, *ApJS*, 183, 67
 Davidge, T. J. 2007, *AJ*, 134, 1799
 de Blok, W. J. G., & Walter, F. 2006, *AJ*, 131, 343
 de Blok, W. J. G., Walter, F., Brinks, E., et al. 2008, *AJ*, 136, 2648
 de Blok, W. J. G., Zwaan, M. A., Dijkstra, M., Briggs, F. H., & Freeman, K. C. 2002, *A&A*, 382, 43
 de Vaucouleurs, G., de Vaucouleurs, A., Corwin, H. G. Jr., et al. 1991, *Third Reference Catalogue of Bright Galaxies* (New York: Springer Verlag)
 Epinat, B., Amram, P., Marcelin, M., et al. 2008, *MNRAS*, 388, 500
 Fingerhut, R. L., Lee, H., McCall, M. L., & Richer, M. G. 2007, *ApJ*, 655, 814
 Fingerhut, R. L., McCall, M. L., Argote, M., et al. 2010, *ApJ*, 716, 792
 Fitzpatrick, E. L. 1999, *PASP*, 111, 63
 Flores, R. A., & Primack, J. R. 1994, *ApJ*, 427, L1
 Flynn, C., Holmberg, J., Portinari, L., Fuchs, B., & Jahreiß, H. 2006, *MNRAS*, 372, 1149
 Gallart, C., Aparicio, A., & Vilchez, J. M. 1996, *AJ*, 112, 1928
 Gibson, B. K. 2000, *Mem. Soc. Astron. Ital.*, 71, 693
 Giovanelli, R., & Haynes, M. P. 1993, *AJ*, 105, 1271
 Governato, F., Brook, C., Mayer, L., et al. 2010, *Nature*, 463, 203
 Green, A. W., Glazebrook, K., McGregor, P. J., et al. 2010, *Nature*, 467, 684
 Grocholski, A. J., Aloisi, A., van der Marel, R. P., et al. 2008, *ApJ*, 686, L79
 Herrnstein, J. R., Moran, J. M., Greenhill, L. J., et al. 1999, *Nature*, 400, 539
 Holmberg, J., Flynn, C., & Portinari, L. 2006, *MNRAS*, 367, 449
 Huchtmeier, W. K., Karachentsev, I. D., Karachentseva, V. E., & Ehle, M. 2000, *A&AS*, 141, 469
 Huchtmeier, W. K., Karachentsev, I. D., & Karachentseva, V. E. 2003, *A&A*, 401, 483
 Huchtmeier, W. K., & Richter, O. G. 1986, *A&AS*, 63, 323
 Izotov, Y. I., & Thuan, T. X. 2010, *ApJ*, 710, L67
 Joy, M., & Lester, D. F. 1988, *ApJ*, 331, 145
 Karachentsev, I. D., Sharina, M. E., Dolphin, A. E., et al. 2002a, *A&A*, 385, 21
 Karachentsev, I. D., Sharina, M. E., Makarov, D. I., et al. 2002b, *A&A*, 389, 812
 Karachentsev, I. D., Sharina, M. E., Dolphin, A. E., et al. 2003a, *A&A*, 398, 467
 Karachentsev, I. D., Makarov, D. I., Sharina, M. E., et al. 2003b, *A&A*, 398, 479
 Karachentsev, I. D., Grebel, E. K., Sharina, M. E., et al. 2003c, *A&A*, 404, 93
 Karachentsev, I. D., Sharina, M. E., Dolphin, A. E., & Grebel, E. K. 2003d, *A&A*, 408, 111
 Karachentsev, I. D., Dolphin, A., Tully, R. B., et al. 2006, *AJ*, 131, 1361
 Karachentsev, I. D., Tully, R. B., Dolphin, A., et al. 2007, *AJ*, 133, 504
 Kirby, E. M., Jerjen, H., Ryder, S. D., & Driver, S. P. 2008, *AJ*, 136, 1866
 Kniazev, A. Y., Brosch, N., Hoffman, G. L., et al. 2009, *MNRAS*, 400, 2054
 Koribalski, B. S., Staveley-Smith, L., Kilborn, V. A., et al. 2004, *AJ*, 128, 16
 Lee, H., McCall, M. L., Kingsburgh, R. L., Ross, R., & Stevenson, C. C. 2003, *AJ*, 125, 146
 Longmore, A. J., Hawarden, T. G., Webster, B. L., Goss, W. M., & Mebold, U. 1978, *MNRAS*, 183, 97P
 Macri, L. M., Stanek, K. Z., Bersier, D., Greenhill, L. J., & Reid, M. J. 2006, *ApJ*, 652, 1133
 McCall, M. L. 2004, *AJ*, 128, 2144
 McConnachie, A. W., Irwin, M. J., Ferguson, A. M. N., et al. 2005, *MNRAS*, 356, 979
 McGaugh, S. S. 2005, *ApJ*, 632, 859
 McGaugh, S. S. 2011, *Physical Review Letters*, 106, 121303
 McGaugh, S. S., Schombert, J. M., Bothun, G. D., & de Blok, W. J. G. 2000, *ApJ*, 533, L99
 McGaugh, S. S., Schombert, J. M., de Blok, W. J. G., & Zgurzsky, M. J. 2010, *ApJ*, 708, L14
 Méndez, B., Davis, M., Moustakas, J., et al. 2002, *AJ*, 124, 213
 Meurer, G. R., Carignan, C., Beaulieu, S. F., & Freeman, K. C. 1996, *AJ*, 111, 1551
 Meyer, M. J., Zwaan, M. A., Webster, R. L., et al. 2004, *MNRAS*, 350, 1195
 Minchin, R. F., Disney, M. J., Boyce, P. J., et al. 2003, *MNRAS*, 346, 787
 Moore, B. 1994, *Nature*, 370, 629
 Nelder, J. A., & Mead, R. 1965, *CompJ*, 7, 308
 Oh, S.-H., de Blok, W. J. G., Brinks, E., Walter, F., & Kennicutt, R. C., Jr. 2011, *AJ*, 141, 193
 Portinari, L., Sommer-Larsen, J., & Tantaló, R. 2004, *MNRAS*, 347, 691
 Portinari, L., Flynn, C., Holmberg, J., Fuchs, B., & Jahreiss, H. 2009, *IAU Symposium*, 254, 53P
 Press, W. H., Flannery, B. P., Teukolsky, S. A., & Vetterling, W. T. 1986, *Numerical Recipes: The Art of Scientific Computing* (Cambridge: Cambridge University Press)
 Rizzi, L., Tully, R. B., Makarov, D., et al. 2007, *ApJ*, 661, 815
 Schlegel, D. J., Finkbeiner, D. P., & Davis, M. 1998, *ApJ*, 500, 525
 Simon, J. D., Bolatto, A. D., Leroy, A., Blitz, L., & Gates, E. L. 2005, *ApJ*, 621, 757
 Sirianni, M., Jee, M. J., Benítez, N., et al. 2005, *PASP*, 117, 1049
 Springob, C. M., Haynes, M. P., Giovanelli, R., & Kent, B. R. 2005, *ApJS*, 160, 149
 Stil, J. M., & Israel, F. P. 2002, *A&A*, 389, 29
 Swaters, R. A., van Albada, T. S., van der Hulst, J. M., & Sancisi, R. 2002, *A&A*, 390, 829
 Swaters, R. A., Sancisi, R., van Albada, T. S., & van der Hulst, J. M. 2009, *A&A*, 493, 871
 Tully, R. B., Rizzi, L., Dolphin, A. E., et al. 2006, *AJ*, 132, 729
 Vaduvescu, O., McCall, M. L., Richer, M. G., & Fingerhut, R. L. 2005, *AJ*, 130, 1593
 Vaduvescu, O., Richer, M. G., & McCall, M. L. 2006, *AJ*, 131, 1318
 Vaduvescu, O., McCall, M. L., & Richer, M. G. 2007, *AJ*, 134, 604
 Vaduvescu, O., & McCall, M. L. 2008, *A&A*, 487, 147
 Verheijen, M. A. W., & Sancisi, R. 2001, *A&A*, 370, 765
 Walter, F., Brinks, E., de Blok, W. J. G., et al. 2008, *AJ*, 136, 2563
 Warren, B. E., Jerjen, H., & Koribalski, B. S. 2004, *AJ*, 128, 1152
 Weldrake, D. T. F., de Blok, W. J. G., & Walter, F. 2003, *MNRAS*, 340, 12
 Wolf, J., Martinez, G. D., Bullock, J. S., et al. 2010, *MNRAS*, 406, 1220

Table 1. Log of Observations

Galaxy	RA (2000)	DEC (2000)	Observatory	Date (UT)	Exposure (s)
ESO 294-10	00:26:33.4	-41:51:19	NTT	Aug 16, 2008	2340
ESO 540-30	00:49:20.9	-18:04:32	NTT	Aug 16, 2008	2340
UGC 685	01:07:22.4	+16:41:04	NTT	Aug 16, 2008	2280
ESO 245-05	01:45:03.7	-43:35:53	BLANCO	Aug 12, 2008	2400
NGC 1311	03:20:06.9	-52:11:08	NTT	Aug 16, 2008	1920
UGC 2684	03:20:23.7	+17:17:45	NTT	Aug 16, 2008	2340
ESO 121-20	06:15:54.2	-57:43:32	BLANCO	Mar 13, 2008	1020
ESO 121-20	BLANCO	Aug 12, 2008	2640
ESO 059-01	07:31:18.2	-68:11:17	BLANCO	Mar 13, 2008	1020
NGC 2915	09:26:11.5	-76:37:35	BLANCO	Mar 13, 2008	1020
Antlia Dwarf	10:04:04.1	-27:19:52	BLANCO	Mar 14, 2008	1980
ESO 215-09	10:57:29.9	-48:10:43	BLANCO	Mar 13, 2008	1980
ESO 320-14	11:37:53.2	-39:13:13	BLANCO	Mar 13, 2008	2340
ESO 379-07	11:54:43.5	-33:33:36	BLANCO	Mar 13, 2008	1980
ESO 443-09	12:54:54.0	-28:20:27	BLANCO	Mar 13, 2008	1980
ESO 381-18	12:44:42.4	-35:58:00	BLANCO	Mar 14, 2008	1020
ESO 321-14	12:13:49.6	-38:13:53	BLANCO	Mar 13, 2008	2220
KK98 182	13:05:02.1	-40:04:58	BLANCO	Mar 14, 2008	1980
KK98 195	13:21:08.2	-31:31:45	NTT	Aug 16, 2008	1500
IC 4247	13:26:44.4	-30:21:45	BLANCO	Mar 14, 2008	1020
ESO 444-78	13:36:31.1	-29:14:06	BLANCO	Mar 13, 2008	1020
HIPASS J1337-39	13:37:25.3	-39:53:48	BLANCO	Mar 13, 2008	1020
HIPASS J1337-39	BLANCO	Aug 12, 2008	1260
IC 4316	13:40:18.4	-28:53:32	BLANCO	Mar 12, 2008	1020
HIPASS J1348-37	13:48:47.0	-37:58:29	BLANCO	Mar 14, 2008	1980
HIPASS J1351-47	13:51:12.0	-46:58:13	BLANCO	Mar 12, 2008	1020
HIPASS J1351-47	BLANCO	Mar 14, 2008	1980
NGC 5408	14:03:20.9	-41:22:40	BLANCO	Aug 11, 2008	1200
PGC 51659	14:28:03.7	-46:18:06	BLANCO	Mar 12, 2008	2580
ESO 137-18	16:20:58.4	-60:29:28	BLANCO	Aug 12, 2008	1260
Sag DIG	19:29:59.0	-17:40:41	BLANCO	Aug 12, 2008	2460
DDO 210	20:46:51.8	-12:50:53	BLANCO	Aug 12, 2008	1260
DDO 210	NTT	Aug 16, 2008	2340
ESO 468-020	22:40:43.9	-30:48:00	NTT	Aug 16, 2008	2280
ESO 149-03	23:52:02.8	-52:34:40	NTT	Aug 16, 2008	2040

Table 2. Measurements for Detected Galaxies

Galaxy	μ_{0K} (mag arcsec ⁻²)	r_{0K} (arcsec)	m_{SK} (mag)	m_{TK} (mag)	PA (deg)	e
(1)	(2)	(3)	(4)	(5)	(6)	(7)
ESO 294-10	20.53	12.2	12.66	12.87	0	0.2
UGC 685	19.74	14.8	11.59	11.72	-55	0.3
ESO 245-05	21.09	30.5	11.57	11.65	-60	0.4
NGC 1311	19.15	22.4	10.72	10.55	+40	0.6
UGC 2684	21.17	11.9	14.10	14.15	-65	0.6
ESO 121-20	20.48	13.4	12.58	12.66	+50	0.3
ESO 059-01	19.89	18.3	11.16	11.23	0	0.2
NGC 2915	17.59	17.6	9.46	9.26	-40	0.5
ESO 320-14	20.31	10.6	12.92	12.81	+90	0.3
ESO 381-18	20.17	8.9	13.16	13.15	+80	0.3
ESO 321-14	20.52	18.3	12.85	12.87	+30	0.7
KK98 182	20.76	8.7	13.81	14.06	+90	0.3
IC 4247	18.77	14.5	11.61	11.64	-30	0.7
ESO 444-78	20.14	13.3	12.61	12.52	+30	0.5
IC 4316	20.32	26.8	11.08	11.09	+45	0.4
NGC 5408	18.90	19.2	10.59	10.69	+75	0.5
ESO 137-18	18.31	24.3	9.48	9.40	+30	0.5
ESO 468-20	21.29	17.4	12.95	13.07	+40	0.4
ESO 149-03	20.07	11.3	13.11	13.22	-30	0.6

Notes. (1) Name of galaxy; (2) Central surface brightness of sech model in K_s ; (3) Scale length of sech model in K_s ; (4) Apparent magnitude of sech model in K_s ; (5) Apparent isophotal magnitude in K_s ; (6) Position angle of major axis (from N through E); (7) Ellipticity of isophotes.

Table 3. Sample for analysis: Extinctions and Distances

Galaxy	$E(B - V)$	A_V^{gal}	A_I^{gal}	$A_{K_s}^{gal}$	I_{TRGB}	$(V - I)_{TRGB}$	$M_{I,TRGB}$	D_{mod}	Source
(1)	(mag)	(mag)	(mag)	(mag)	(mag)	(mag)	(mag)	(mag)	(10)
Cam B	0.219	0.695	0.394	0.082	23.60	1.65	-3.92	27.52	1
CGCG 087-33	0.032	0.102	0.058	0.012	25.47	1.15	-4.03	29.50	2
DDO 006	0.017	0.054	0.031	0.006	23.57	1.48	-3.96	27.53	3
DDO 047	0.033	0.105	0.059	0.012	25.48	1.13	-4.04	29.52	2
DDO 099	0.026	0.083	0.047	0.010	23.11	1.29	-4.00	27.11	4
DDO 167	0.010	0.032	0.018	0.004	24.06	1.49	-3.96	28.02	5
DDO 168	0.015	0.048	0.027	0.006	24.13	1.40	-3.98	28.11	5
DDO 181	0.006	0.019	0.011	0.002	23.46	1.35	-3.99	27.45	4
DDO 187	0.023	0.073	0.041	0.009	22.69	1.34	-3.99	26.68	4
DDO 190	0.012	0.039	0.022	0.005	23.19	1.38	-3.98	27.17	4
DDO 226	0.015	0.049	0.028	0.006	24.41	1.47	-3.96	28.37	3
ESO 059-01	0.147	0.467	0.265	0.055	24.26	1.54	-3.95	28.21	6
ESO 121-20	0.042	0.132	0.075	0.016	24.86	1.33	-3.99	28.86	6
ESO 137-18	0.245	0.777	0.441	0.092	25.01	1.55	-3.95	28.95	7
ESO 215-09	0.221	0.700	0.397	0.083	24.58	1.43	-3.97	28.55	7
ESO 223-09	0.260	0.824	0.467	0.097	25.04	1.59	-3.94	28.98	7
ESO 269-58	0.109	0.345	0.196	0.041	23.86	1.61	-3.93	27.80	8
ESO 320-14	0.143	0.454	0.257	0.053	24.89	1.45	-3.97	28.86	7
ESO 321-14	0.094	0.299	0.170	0.035	23.51	1.34	-3.99	27.50	4
ESO 324-24	0.113	0.358	0.203	0.042	23.81	1.43	-3.97	27.79	9
ESO 325-11	0.088	0.279	0.158	0.033	23.62	1.36	-3.99	27.61	9
ESO 349-31	0.012	0.038	0.022	0.004	23.48	1.43	-3.97	27.45	6
ESO 379-07	0.074	0.236	0.134	0.028	24.54	1.59	-3.94	28.48	9
ESO 381-18	0.063	0.199	0.113	0.023	24.58	1.46	-3.97	28.55	7
ESO 381-20	0.066	0.208	0.118	0.024	24.64	1.42	-3.98	28.61	7
ESO 384-16	0.074	0.235	0.133	0.028	24.23	1.55	-3.95	28.18	7
ESO 444-78	0.053	0.167	0.095	0.020	24.55	1.42	-3.97	28.53	7
ESO 444-84	0.069	0.218	0.123	0.026	24.27	1.29	-4.00	28.28	9
ESO 461-36	0.303	0.962	0.546	0.114	25.45	1.32	-4.00	29.45	6
GR 8	0.026	0.082	0.046	0.010	22.63	2.21	-3.80	26.43	2
Ho II	0.032	0.101	0.057	0.012	23.61	1.41	-3.98	27.59	4
IC 3104	0.410	1.301	0.739	0.154	22.75	1.29	-4.00	26.75	10
IC 4247	0.065	0.205	0.116	0.024	24.43	1.39	-3.98	28.41	7
IC 4316	0.055	0.173	0.098	0.020	24.10	1.72	-3.91	28.01	9
IC 4662	0.070	0.222	0.126	0.026	22.89	1.64	-3.93	26.82	6
IC 5152	0.025	0.079	0.045	0.009	22.42	1.58	-3.94	26.36	2
KK98 17	0.055	0.173	0.098	0.020	24.41	1.07	-4.05	28.46	2
KK98 182	0.102	0.325	0.184	0.038	24.77	1.29	-4.00	28.77	7
KK98 200	0.069	0.219	0.124	0.026	24.20	1.60	-3.93	28.14	9
KK98 230	0.014	0.045	0.025	0.005	22.47	1.31	-4.00	26.47	4
KKH 086	0.027	0.085	0.048	0.010	23.09	1.32	-4.00	27.08	4
KKH 098	0.123	0.389	0.221	0.046	22.92	1.49	-3.96	26.88	10
Mrk 178	0.019	0.060	0.034	0.007	23.90	1.49	-3.96	27.86	5
NGC 1311	0.022	0.068	0.039	0.008	24.63	1.15	-4.03	28.66	2
NGC 1569	0.694	2.206	1.254	0.262	23.12	1.36	-3.99	27.10	11
NGC 2915	0.275	0.872	0.495	0.103	23.87	1.76	-3.90	27.77	12
NGC 3077	0.067	0.212	0.120	0.025	23.93	1.77	-3.90	27.82	4
NGC 3738	0.010	0.033	0.019	0.004	24.40	1.75	-3.90	28.30	5
NGC 4163	0.020	0.063	0.036	0.007	23.27	1.44	-3.97	27.24	4
NGC 4214	0.022	0.069	0.039	0.008	23.43	1.47	-3.96	27.39	4
NGC 5408	0.068	0.216	0.123	0.025	24.36	0.90	-4.09	28.45	9
NGC 6822	0.231	0.732	0.415	0.086	19.39	1.58	-3.94	23.32	13
Peg DIG	0.068	0.216	0.122	0.025	20.75	1.52	-3.95	24.70	14
Sex A	0.045	0.141	0.080	0.017	21.76	1.23	-4.02	25.77	4
Sex B	0.031	0.099	0.056	0.012	21.77	1.35	-3.99	25.76	4
UGC 0685	0.057	0.182	0.103	0.021	24.32	1.12	-4.04	28.36	2
UGC 3755	0.088	0.280	0.159	0.033	25.31	1.08	-4.05	29.36	2
UGC 4115	0.028	0.090	0.051	0.011	25.39	1.04	-4.06	29.44	2
UGC 4483	0.034	0.108	0.061	0.013	23.72	1.23	-4.02	27.74	4
UGC 6456	0.037	0.119	0.067	0.014	24.20	1.38	-3.98	28.19	15
UGC 7605	0.015	0.046	0.026	0.005	24.18	1.34	-3.99	28.17	5
UGC 8508	0.015	0.048	0.027	0.006	22.99	1.38	-3.98	26.98	10
UGC 8833	0.012	0.037	0.021	0.004	23.41	1.36	-3.99	27.40	4
UGCA 092	0.785	2.496	1.420	0.296	23.46	1.18	-4.03	27.49	6

Table 3. continued.

Galaxy	$E(B - V)$ (mag)	A_V^{gal} (mag)	A_I^{gal} (mag)	$A_{K_s}^{gal}$ (mag)	I_{TRGB} (mag)	$(V - I)_{TRGB}$ (mag)	$M_{I,TRGB}$ (mag)	D_{mod} (mag)	Source
(1)	(2)	(3)	(4)	(5)	(6)	(7)	(8)	(9)	(10)
UGCA 438	0.015	0.046	0.026	0.005	22.69	1.37	-3.98	26.67	4
WLM	0.038	0.120	0.068	0.014	20.85	1.47	-3.96	24.82	16

Notes. (1) Name of galaxy; (2) Galactic colour excess from Schlegel et al. (1998); (3) Galactic extinction of M0 III star in V; (4) Galactic extinction of M0 III star in I; (5) Galactic extinction of dwarf irregular galaxy in K_s ; (6) I magnitude of stars at tip of red giant branch, corrected for extinction and redshift; (7) $(V - I)$ colour of stars at tip of red giant branch, corrected for extinction and redshift; (8) Absolute magnitude of TRGB stars in I ; (9) Distance modulus; (10) Source of colour-magnitude diagram.

References. (1) Karachentsev et al. (2003d); (2) Tully et al. (2006); (3) Karachentsev et al. (2003c); (4) Dalcanton et al. (2009); (5) Karachentsev et al. (2003a); (6) Karachentsev et al. (2006); (7) Karachentsev et al. (2007); (8) Davidge (2007); (9) Karachentsev et al. (2002a); (10) Karachentsev et al. (2002b); (11) Grocholski et al. (2008); (12) Karachentsev et al. (2003b); (13) Gallart et al. (1996); (14) McConnachie et al. (2005); (15) Méndez et al. (2002); (16) Rizzi et al. (2007).

Table 4. Sample for Analysis: Radio and Optical Parameters

Galaxy	V_{\odot} (km s^{-1})	F_{HI} (Jy km s^{-1})	W_{20}^{app} (km s^{-1})	R (km s^{-1})	$\log W_{20}$ (km s^{-1})	HI Source	μ_0 (mag arcsec^{-2})	$r_{0,\text{pc}}$ (pc)	q	r_{rim}/r_0	Photometry Source
(1)	(2)	(3)	(4)	(5)	(6)	(7)	(8)	(9)	(10)	(11)	(12)
Cam B	78	5.0	32.6	1.65	1.512	H1, H2, H3	21.87	407	0.44	2.40	P1
CGCG 087-33	279	2.6	55.8	1.4	1.746	H1	19.74	532	0.41	4.13	P2
DDO 006	295	3.4	32.9	1.4	1.516	H1	22.04	570	0.29	2.53	P3
DDO 047	272	61.4	111.0	2.06	2.045	H4	21.78	555	1.00	4.20	P4
DDO 099	243	46.0	91.0	2.06	1.958	H4	21.30	393	0.71	2.67	P1
DDO 167	163	4.6	40.2	1.4	1.604	H1	21.65	337	0.60	3.47	P4
DDO 168	191	74.4	88.0	8.24	1.940	H5, H6	20.36	733	0.38	3.96	P1
DDO 181	202	11.4	56.8	1.4	1.754	H1	20.77	356	0.70	2.87	P1
DDO 187	153	12.0	51.4	1.4	1.710	H1	21.71	287	0.60	3.68	P4
DDO 190	151	27.1	64.0	8.24	1.797	H5, H6	19.62	257	0.89	4.21	P1
DDO 226	359	6.1	56.4	1.65	1.750	H7, H3	20.58	982	0.15	3.05	P3
ESO 059-01	530	17.7	104.0	18	2.001	H8	19.84	389	0.80	4.92	P5
ESO 121-20	577	14.1	96.0	18	1.963	H8	20.47	384	0.70	4.48	P5
ESO 137-18	605	37.4	155.0	18	2.183	H8	18.22	727	0.50	6.17	P5
ESO 215-09	597	122.0	93.0	4	1.967	H9	20.90	430	0.83	3.49	P6
ESO 223-09	593	96.2	103.0	8.2	2.009	H10	19.21	1044	0.70	4.35	P7
ESO 269-58	400	7.2	84.0	18	1.899	H11	19.10	636	0.63	4.72	P3
ESO 320-14	654	2.5	61.3	18	1.738	H7	20.26	304	0.70	4.25	P7
ESO 321-14	609	6.4	29.0	1.65	1.459	H8, H3	21.18	522	0.27	2.59	P6
ESO 324-24	526	52.1	113.0	8.2	2.050	H10	20.43	630	0.93	3.13	P6
ESO 325-11	550	25.4	77.0	8.2	1.880	H10	20.93	775	0.35	3.13	P3
ESO 349-31	229	2.7	31.0	8.2	1.453	H10	21.51	323	0.58	3.21	P3
ESO 379-07	644	5.2	40.0	1.65	1.600	H8, H3	22.10	443	0.85	2.81	P6
ESO 381-18	625	3.3	61.6	18	1.741	H7	20.29	224	0.70	4.77	P6, P5
ESO 381-20	596	31.9	103.0	8.2	2.009	H10	20.99	891	0.32	2.89	P8
ESO 384-16	504	1.5	41.0	1.2	1.612	H12	19.45	214	0.92	3.00	P6
ESO 444-78	573	4.0	52.1	1.4	1.716	H1	20.46	475	0.41	3.00	P1
ESO 444-84	583	21.1	75.0	4	1.873	H8, H13	20.60	318	0.89	2.46	P1
ESO 461-36	427	7.5	84.0	10.2	1.916	H7, H14	20.51	492	0.50	4.58	P7
GR 8	214	7.8	39.2	1.4	1.592	H1	21.36	152	0.80	3.70	P4
Ho II	156	267.0	72.0	5.2	1.854	H15	19.66	1348	1.00	2.25	P9
IC 3104	429	10.3	63.0	18	1.753	H8	18.85	468	0.45	3.42	P3
IC 4247	419	3.4	49.0	18	1.608	H16	18.77	370	0.33	5.30	P2, P5
IC 4316	576	2.1	32.8	1.65	1.513	H16, H3	20.31	520	0.60	4.47	P5
IC 4662	302	130.0	133.0	18	2.114	H8	17.40	242	0.73	5.69	P3
IC 5152	122	97.2	100.0	18	1.983	H8	18.08	345	0.66	5.22	P3
KK98 17	156	1.0	53.0	10.2	1.705	H14	21.67	470	0.31	2.98	P10
KK98 182	613	2.1	24.0	7.9	1.316	H14	21.28	400	0.68	3.07	P3
KK98 200	494	1.7	26.5	1.65	1.421	H1, H3	20.51	179	0.70	5.17	P7
KK98 230	63	2.6	25.9	1.65	1.411	H1, H17	22.57	140	0.95	1.76	P11
KKH 086	287	0.5	20.6	1.4	1.310	H1	21.56	181	0.61	1.98	P3
KKH 098	-132	4.1	31.5	1.65	1.498	H1, H3	21.39	184	0.59	2.68	P10
Mrk 178	250	3.0	44.8	1.4	1.650	H1	19.15	228	0.50	5.56	P4
NGC 1311	568	14.6	105.0	18	2.005	H8	19.15	586	0.40	5.36	P12
NGC 1569	-86	84.0	123.8	5.2	2.092	H18	16.83	271	0.55	6.13	P4
NGC 2915	468	145.0	163.0	6.6	2.211	H19	17.49	306	0.50	7.67	P5
NGC 3077	-20	256.0	157.3	5.2	2.196	H18	17.28	593	0.70	4.50	P9
NGC 3738	225	22.0	122.0	8.24	2.084	H6	18.41	437	0.70	5.08	P4
NGC 4163	164	9.6	38.0	4.1	1.574	H5, H20	19.29	223	0.70	5.18	P4
NGC 4214	293	319.8	89.8	2.6	1.952	H5, H18	17.63	491	0.50	4.46	P9
NGC 5408	506	65.5	123.0	8.2	2.087	H10	18.88	456	0.50	7.03	P5
NGC 6822	-55	2266.0	115.0	1.9	2.061	H21, H22	19.55	239	0.80	1.87	P9
Peg DIG	-183	28.1	38.6	5.3	1.577	H23	20.93	333	0.55	2.08	P10
Sex A	324	168.0	64.0	1.12	1.806	H24	21.09	362	0.95	3.03	P3
Sex B	301	72.9	56.0	1.4	1.747	H1	20.57	255	0.87	3.53	P6
UGC 0685	156	13.4	83.0	1.65	1.919	H25, H3	19.72	336	0.70	5.07	P12
UGC 3755	315	6.8	50.6	1.4	1.703	H1	19.81	808	0.50	3.72	P2
UGC 4115	343	21.0	106.0	1.65	2.025	H5, H3	20.24	803	0.40	3.74	P4
UGC 4483	156	13.6	50.6	1.4	1.703	H1	20.70	306	0.55	2.81	P1
UGC 6456	-94	10.1	52.0	1.65	1.716	H3	20.16	248	0.70	5.08	P4
UGC 7605	310	5.7	43.7	1.4	1.640	H1	20.75	402	0.67	3.91	P11
UGC 8508	56	18.3	65.0	1.65	1.813	H3	19.95	234	0.55	4.64	P13
UGC 8833	227	6.0	42.8	1.4	1.631	H1	20.94	274	0.77	4.05	P2
UGCA 092	-95	104.7	73.0	1.65	1.863	H5, H3	20.53	635	0.50	2.40	P4

Table 4. continued.

Galaxy	V_{\odot} (km s^{-1})	F_{HI} (Jy km s^{-1})	W_{20}^{app} (km s^{-1})	R (km s^{-1})	$\log W_{20}$ (km s^{-1})	HI Source	μ_0 (mag arcsec^{-2})	$r_{0,pc}$ (pc)	q	r_{lim}/r_0	Photometry Source
(1)	(2)	(3)	(4)	(5)	(6)	(7)	(8)	(9)	(10)	(11)	(12)
UGCA 438	62	15.0	35.0	8.2	1.514	H26	20.48	283	0.90	3.97	P3
WLM	-122	292.0	81.0	1.12	1.909	H24	21.28	437	0.40	3.06	P7

Notes. (1) Name of galaxy; (2) Heliocentric radial velocity defined by HI; (3) Integrated HI flux; (4) Apparent full width of 21 cm line at 20% of peak; (5) FWHM of instrumental profile; (6) Logarithm of the 21 cm line width at 20% of peak, corrected for instrumental broadening and redshift; (7) Source of HI data; (8) Central surface brightness of sech model, corrected for extinction and redshift; (9) Scale length of sech model in parsecs; (10) Adopted ratio of minor to major axes of isophotes; (11) Ratio of radius of limiting isophote to scale length of sech; (12) Source of surface photometry.

References. (H1) Huchtmeier et al. (2003); (H2) Begum et al. (2003); (H3) Begum et al. (2008); (H4) Springob et al. (2005); (H5) Huchtmeier & Richter (1986); (H6) Stil & Israel (2002); (H7) Meyer et al. (2004); (H8) Koribalski et al. (2004); (H9) Warren et al. (2004); (H10) Cote et al. (1997); (H11) Banks et al. (1999); (H12) Beaulieu et al. (2006); (H13) de Blok et al. (2002); (H14) Huchtmeier et al. (2000); (H15) Bureau & Carignan (2002); (H16) Minchin et al. (2003); (H17) Begum et al. (2006); (H18) Walter et al. (2008); (H19) Meurer et al. (1996); (H20) Swaters et al. (2002); (H21) de Blok & Walter (2006); (H22) Weldrake et al. (2003); (H23) Kniazev et al. (2009); (H24) Barnes & de Blok (2004); (H25) Giovanelli & Haynes (1993) (H26) Longmore et al. (1978); (P1) CFHT 2004: Fingerhut et al. (2010); (P2) SPM 2005: Fingerhut et al. (2010); (P3) IRSF 2006: Fingerhut et al. (2010); (P4) CFHT 2002: Vaduvescu et al. (2005); (P5) CTIO 2008: this paper; (P6) IRSF 2005: Fingerhut et al. (2010); (P7) CTIO 2007: Vaduvescu & McCall (2008); (P8) CTIO 2006: Fingerhut et al. (2010); (P9) 2MASS: Vaduvescu & McCall (2008); (P10) CFHT 2005: Fingerhut et al. (2010); (P11) CFHT 2006: Fingerhut et al. (2010); (P12) ESO 2008: this paper; (P13) SPM 2002: Vaduvescu et al. (2005).

Table 5. Sample for Analysis: Derived Global Properties

Galaxy	Weight	M_{K_s} (mag)	L_{burst}/L_{sech}	$\log M_{gas}$ (M_{\odot})	$\log M_{stars}$ (M_{\odot})	$\log M_{bary}$ (M_{\odot})	Gas Fraction	$\log P$ ($M_{\odot} \text{pc}^{-1}$)	M/L (virial) (M_{\odot}/L_{\odot})
(1)	(2)	(3)	(4)	(5)	(6)	(7)	(8)	(9)	(10)
Cam B	0	-14.51	0.010	7.213	7.077	7.451	0.578	4.842	2.95
CGCG 087-33	1	-17.15	0.000	7.722	8.131	8.274	0.281	5.548	0.88
DDO 006	1	-14.62	0.000	7.049	7.122	7.388	0.458	4.632	5.28
DDO 047	0	-16.17	0.000	9.100	7.738	9.119	0.958	6.374	5.65
DDO 099	1	-15.52	0.017	8.012	7.481	8.124	0.772	5.530	3.98
DDO 167	1	-14.66	0.000	7.377	7.137	7.575	0.635	5.047	2.30
DDO 168	0	-17.14	0.000	8.622	8.130	8.743	0.756	5.878	2.95
DDO 181	1	-15.82	0.003	7.544	7.602	7.875	0.467	5.324	1.36
DDO 187	1	-14.24	0.000	7.259	6.969	7.439	0.661	4.982	3.33
DDO 190	1	-16.53	0.000	7.807	7.884	8.148	0.456	5.738	0.42
DDO 226	1	-16.55	0.000	7.641	7.891	8.085	0.360	5.093	5.27
ESO 059-01	1	-17.09	0.000	8.038	8.109	8.376	0.459	5.786	1.04
ESO 121-20	1	-16.29	0.000	8.198	7.787	8.340	0.720	5.756	1.90
ESO 137-18	1	-19.56	0.059	8.660	9.095	9.231	0.269	6.369	0.64
ESO 215-09	0	-16.29	0.000	9.013	7.788	9.038	0.944	6.404	2.42
ESO 223-09	0	-19.72	0.000	9.080	9.162	9.424	0.453	6.405	0.68
ESO 269-58	1	-18.64	0.258	7.482	8.727	8.751	0.054	5.948	0.50
ESO 320-14	1	-15.99	0.000	7.447	7.667	7.872	0.376	5.389	0.81
ESO 321-14	1	-15.21	0.012	7.311	7.357	7.636	0.474	4.918	2.18
ESO 324-24	1	-17.71	0.000	8.337	8.356	8.648	0.489	5.849	1.78
ESO 325-11	1	-16.60	0.000	7.954	7.912	8.234	0.524	5.345	4.57
ESO 349-31	1	-14.68	0.000	6.917	7.142	7.345	0.373	4.835	1.35
ESO 379-07	1	-15.18	0.014	7.614	7.345	7.801	0.650	5.155	2.44
ESO 381-18	1	-15.29	0.000	7.444	7.390	7.719	0.531	5.369	0.84
ESO 381-20	1	-16.75	0.000	8.455	7.971	8.579	0.753	5.629	7.68
ESO 384-16	1	-16.34	0.045	6.962	7.807	7.865	0.125	5.535	0.20
ESO 444-78	1	-16.18	0.000	7.518	7.745	7.948	0.372	5.271	1.56
ESO 444-84	0	-16.01	0.000	8.140	7.676	8.269	0.745	5.767	1.30
ESO 461-36	1	-16.42	0.000	8.160	7.842	8.330	0.675	5.638	2.41
GR 8	1	-13.53	0.000	6.972	6.684	7.153	0.660	4.970	1.28
Ho II	0	-20.21	0.000	8.969	9.358	9.507	0.290	6.377	0.46
IC 3104	1	-17.86	0.000	7.219	8.416	8.442	0.060	5.772	0.36
IC 4247	1	-17.06	0.000	7.403	8.097	8.177	0.168	5.608	0.30
IC 4316	1	-16.94	0.109	7.031	8.050	8.089	0.087	5.374	0.51
IC 4662	1	-18.41	0.000	8.347	8.634	8.815	0.341	6.431	0.17
IC 5152	1	-18.38	0.077	8.039	8.625	8.725	0.206	6.187	0.24
KK98 17	0	-14.64	0.005	6.868	7.129	7.319	0.354	4.647	6.11
KK98 182	0	-15.54	0.000	7.342	7.487	7.722	0.417	5.120	0.62
KK98 200	1	-14.59	0.000	6.992	7.109	7.356	0.433	5.103	0.41
KK98 230	0	-12.34	0.015	6.508	6.207	6.684	0.667	4.537	1.93
KKH 086	0	-13.42	0.000	6.039	6.638	6.736	0.201	4.478	0.89
KKH 098	1	-13.59	0.000	6.870	6.706	7.097	0.593	4.832	1.36
Mrk 178	1	-16.12	0.000	7.128	7.720	7.819	0.204	5.461	0.32
NGC 1311	1	-17.92	0.194	8.135	8.442	8.616	0.330	5.848	1.11
NGC 1569	1	-18.91	0.348	8.272	8.837	8.941	0.214	6.509	0.12
NGC 2915	0	-18.41	0.000	8.777	8.636	9.013	0.580	6.527	0.35
NGC 3077	0	-20.43	0.107	9.044	9.443	9.589	0.285	6.816	0.20
NGC 3738	1	-18.63	0.204	8.169	8.725	8.831	0.218	6.191	0.40
NGC 4163	1	-16.28	0.000	7.383	7.785	7.930	0.284	5.582	0.21
NGC 4214	0	-19.29	0.016	8.969	8.989	9.280	0.488	6.589	0.19
NGC 5408	1	-17.89	0.000	8.703	8.428	8.888	0.653	6.229	0.88
NGC 6822	0	-16.32	0.000	8.191	7.802	8.339	0.710	5.960	0.95
Peg DIG	0	-15.25	0.000	6.835	7.374	7.484	0.224	4.962	1.20
Sex A	1	-15.87	0.000	8.040	7.622	8.180	0.723	5.622	1.56
Sex B	1	-15.53	0.000	7.673	7.485	7.890	0.606	5.484	0.90
UGC 0685	1	-16.75	0.000	7.975	7.973	8.275	0.501	5.748	0.84
UGC 3755	0	-18.20	0.000	8.082	8.552	8.679	0.253	5.771	0.68
UGC 4115	1	-17.51	0.000	8.606	8.277	8.773	0.681	5.868	3.23
UGC 4483	1	-15.31	0.000	7.734	7.395	7.898	0.686	5.412	1.40
UGC 6456	1	-15.66	0.000	7.785	7.535	7.979	0.640	5.584	0.69
UGC 7605	1	-16.06	0.000	7.532	7.697	7.923	0.406	5.319	1.00
UGC 8508	1	-15.46	0.000	7.559	7.457	7.812	0.558	5.443	0.97
UGC 8833	1	-15.19	0.000	7.244	7.349	7.601	0.440	5.163	1.01
UGCA 092	0	-16.95	0.000	8.520	8.054	8.648	0.745	5.845	2.11

Table 5. continued.

Galaxy	Weight	M_{K_s} (mag)	L_{burst}/L_{sech}	$\log M_{gas}$ (M_{\odot})	$\log M_{stars}$ (M_{\odot})	$\log M_{bary}$ (M_{\odot})	Gas Fraction	$\log P$ ($M_{\odot} \text{pc}^{-1}$)	M/L (virial) (M_{\odot}/L_{\odot})
(1)	(2)	(3)	(4)	(5)	(6)	(7)	(8)	(9)	(10)
UGCA 438	1	-15.89	0.000	7.350	7.629	7.812	0.345	5.361	0.40
WLM	1	-15.15	0.000	7.898	7.331	8.002	0.787	5.361	6.02

Notes. (1) Name of galaxy; (2) Weight during fitting; (3) Absolute magnitude of sech model in K_s ; (4) Luminosity of burst relative to luminosity of sech model; (5) Logarithm of the gas mass; (6) Logarithm of the mass of stars in the sech model, computed assuming a fixed mass-to-light ratio of 0.883 in K_s ; (7) Logarithm of the baryonic mass (sum of gaseous and stellar masses); (8) Gas fraction (for a fixed mass-to-light ratio of 0.883 in K_s); (9) Logarithm of the potential defined by the ratio of the baryonic mass to the scale length of the sech model; (10) Mass-to-light ratio of the stars in K_s as indicated by the deviation of the surface brightness from the norm for a virialized system.